Article

Simulations of Mesoscale Flow Systems around Dugway Proving Ground Using the WRF Modeling System

Robert E. Dumais, Jr. [1,*], Daniela M. Spade [2] and Thomas E. Gill [3]

1 U.S. Army Combat Capabilities Development Command Army Research Laboratory, White Sands Missile Range, NM 88002, USA
2 Department of Geography and Environmental Sustainment, University of Oklahoma, Norman, OK 73019, USA
3 Department of Earth, Environmental and Resource Sciences, University of Texas-El Paso, El Paso, TX 79968, USA
* Correspondence: robert.e.dumais.civ@army.mil; Tel.: +1-575-694-5022

Abstract: It is widely recognized that regions with complex heterogeneous topography and land-use properties produce a variety of diurnal mesoscale and microscale flows, which can be modified or even masked by significant large-scale synoptic forcing. These flows can be produced through both dynamic and thermal-forcing processes. Recent field programs such as the Terrain-induced Rotor Experiment (T-REX), Mountain Terrain Atmospheric Modeling and Observations Program (MATERHORN), and Perdigao have been used to observe and model flow behaviors under different topographical and large-scale meteorological conditions. Using the Advanced research version of the Weather Research and Forecast (WRF-ARW) model, we applied multi-nesting using an interactive one-way nesting approach to resolve to a sub-kilometer inner-grid spacing (0.452 km). Our interest was in the intensive observation period 6 (IOP6) of the Fall 2012 MATERHORN campaign conducted over Dugway Proving Ground (DPG) in Utah. An initial review of the IOP6 suggested that a range of diurnal flows were present, and that a relatively small subset of model setup configurations would be able to capture the general flows of this period. The review also led us to believe that this same subset would be able to capture differences due to variations in choice of model boundary-layer physics, land surface physics, land use/soil type specifications, and larger-scale meteorological conditions. A high model vertical resolution was used, with 90 vertical sigma levels applied. The IOP6 spanned the period of 2012 0800 UTC 14 October–0800 UTC 15 October. Based upon a lack of deep convection and moist microphysics throughout IOP6, we included comparison of planetary boundary layer (PBL) turbulence parameterization schemes even at the sub-kilometer grid spacing. We focused upon the gross model performance over our inner nest; therefore, a detailed comparison of the effects of model horizontal resolution are excluded. For surface parameters of wind and temperature, we compare mean absolute error and bias scores throughout the period at a number of surface meteorological observing sites. We found that despite attention given to the boundary layer turbulence physics, radiation physics and model vertical resolution, the results seemed to indicate more impact from the choices of thermal soil conductivity parameterization, land surface/soil texture category classification (and associated static property-parameter values), and large-scale forcing model. This finding lends support to what other researchers have found related to how these same forcings can exert a strong influence upon mesoscale flows around DPG. Our findings suggest that the two nights of IOP6 offer a pair of excellent consecutive nights to explore many of the forcing features important to local complex terrain flow. The flows of interest in this case included valley, anabatic/katabatic, and playa breeze systems. Subjective evidence was also found to support an influence provided by the modest synoptic northwesterly flow present within the lower troposphere (mainly on the night of 14 October). Follow-on research using the WRF-ARW capability to nest directly from mesoscale-to-LES can leverage IOP6 further. For example, to uncover more detailed and focused aspects of the dynamic and thermodynamic forcings contributing to the DPG diurnal flows.

Keywords: mesoscale; flow; simulation; MATERHORN; terrain; landuse

1. Introduction

The WRF-ARW (hereafter just WRF) [1] is a numerical weather prediction (NWP) system that resolves scales of meteorological phenomena ranging from synoptic to meso-gamma serving both atmospheric research and operational forecasting needs. Throughout a WRF simulation, land-cover properties play an important role by determining the surface soil moisture, albedo, and roughness length which influence the surface heat budget for computing fluxes [2,3]. To accurately reproduce mesoscale flows, the model (through its user-defined name list) must select an appropriate suite of available model physics options (which are simplified parameterizations of complex and/or subgrid processes such as boundary layer turbulence), determine the appropriate type of averaging applied to the underlying topography (dependent upon spatial resolution desired in model), and accurately represent the dominant surface land cover and soil properties. Simulations here were executed using the older WRF v3.6.1 due to it being the official organizational version supported at the time of the original research underlying this paper. It is understood that this could be seen as a point of some concern, although a more recent single simulation tested using v4.1.2 (not shown) showed little significant difference from the overall gross model results that are presented here. Since the time of v3.6.1, some of the more significant model upgrades have been associated with the vertical coordinate and vertical nesting. These will be discussed as future emphasis for LES work being planned later.

1.1. Review of Diurnal Flows Found over DPG

Katabatic (downslope drainage) and anabatic (upslope) winds are a commonly observed pair of diurnal flows around DPG, which are forced by thermodynamic gradients along sloped surfaces. These diurnal flows are prevalent along the higher terrain that surrounds all four borders of the Great Salt Desert (GSD). Numerous topographical features are located around the periphery of the expansive GSD (Deep Creek Mountains, Silver Island Mountains, Goshute Mountains, Dutch Mountain, Pilot Range, Newfoundland Mountains, Grouse Creek Mountains, Raft River Mountains, Terrace Mountain, Grassy Mountains, Lakeside Mountains, Cedar Mountains, Granite Peak, Dugway Range, Thomas Range, and Fish Springs Range). On sloping terrain such as along mountains, hills, ridges, and valley sidewalls, the nocturnal radiative flux divergence at the surface induces katabatic "downslope" drainage flows almost immediately after the removal of solar heating. The slope angle greatly influences the inversion depth that will develop, with the colder air near the surface (relative to the same height in the nearby free atmosphere) creating a pressure gradient sufficient to cause the drainage [4,5]. Katabatic flows typically have their greatest magnitude at some level just above the ground, despite the largest temperature differences (and resultant pressure gradients) being at the surface level. This is due to surface friction acting to retard the flow right at ground level.

Excellent reviews of katabatic flow are given in [4,6,7]. The paper of [8] argues that the shallow (2 m AGL) nocturnal downslope katabatic flow begins to exceed that a little higher up (20 m AGL) typically a few hours after shadowing (around time of max cooling rate) occurs. Observations indicate a generally unsteady nature to these flows unlike what may be expected under a purely theoretical slope-driven consideration [6,9–12]. Nonlinear interactions in complex terrain between mountain waves and katabatic flows (driven by dynamic pressure effects) have been shown to be contributors to observed unsteadiness of katabatic flow [13]. Similar interactions appear to occur in the region around DPG [14,15]. The anabatic flow component is the daytime reversal of the nighttime katabatic flow, which are forced by surface solar heating along the sloping terrain [5,16]. The surface solar-radiation loading after daybreak quickly heats the sloped terrain, which induces a pressure gradient that forces air flow to move up the slope [17]. These daytime flows can serve as a preferred mechanism for the initiation of local convection such as in the Southwest U.S. monsoon season [18]. Within steep and narrow valley locations, anabatic flows become more pronounced in the mid–late morning hours [9].

After the late morning (late evening) hours, slope-driven flows (to that point generally perpendicular to the main valley axis) tend to become dominated by a deepening upvalley (downvalley) wind system which flows close to parallel with the valley axis. This is especially true for deeper three-dimensional valley systems. Valley flows are produced by along-valley thermodynamically induced pressure gradients, where the magnitudes are largely determined using valley width, depth, and slope [16,19–21]. During the night, the smaller volume of air within the valley interior cools faster, resulting in a pressure gradient forcing a downvalley flow nearly parallel to the valley orientation (flow from interior of valley towards valley entrance onto the plain). Similarly, the volume of interior valley air warms more during the daytime, which causes a reversal of the pressure gradient and the flow to one that is upvalley (flow from valley entrance up through the interior). In [22], a study was conducted in which high spatio-temporal resolution wind data was collected near DPG to verify the WRF model output for the area. The study investigated the atmospheric boundary layer around Granite Mountain. The high spatio-temporal resolution wind data was collected via a Twin Otter Doppler Wind Lidar. This data revealed a recurring pattern of thermally driven daytime upvalley flow coming out of the north and flowing around Granite Mountain.

A playa (or salt) breeze is a thermally forced direct circulation [23] that develops near the edges of playas (dry salt lakes) since they have properties distinct from the surrounding land cover [15,24]. These are quite similar to a sea or lake breeze system. The properties of playas include a higher thermal conductivity, greater sensible heat flux, higher albedo due to the presence of a thin salt crust at the surface, sparser vegetation cover relative to the surrounding land cover, and at times a somewhat higher latent heat flux relative to the surrounding desert land cover [15]. The combination of these characteristics results in differential heating and a local thermally direct circulation, with low-level flow directed away from the playa during the day (playa surface cooler than over surrounding land cover) and toward the playa at night (playa surface warmer than over surrounding land cover) [15,24]. The magnitude of the surface temperature difference between playa/off-playa controls the strength of the playa flow system on any given day. The extent of any identifiable upper-level return circulation is usually deeper in the afternoon (up to 250 m AGL or greater) than at night (100 m AGL), due to the usual nocturnal static stability found close to the ground [15,24,25]. Studies of the playa breeze over Utah [15] have indicated that the daytime circulation depth may be even higher within a convective boundary layer. Previous studies have shown that surface temperature gradients between the playa and surrounding land cover are greater during the day then at night. In [24], the recorded albedo values were almost 60% on a playa surface versus 32% on the surrounding land cover. This gradient in albedo values resulted in a daytime temperature of 40 °C on the surrounding land cover and 24 °C on the playa surface, whereas nighttime temperature differences were significantly smaller with values of 0.4 °C on the non-playa land cover and 8 °C on the playa surface. It was concluded in [25] that the playa breeze resulted largely from the differences in albedo between the playa and surrounding land cover rather than from differences in the soil thermal properties.

1.2. Influence of Land Use and Soil on Diurnal Flows

The study of [26] investigated the effect that improved land-use information had on the WRF model's ability to predict changes in potential temperature, mixing ratio, and ozone with height. Their WRF simulations were setup with a much higher resolution set of land-use information than that previously available. To test the new data, they first released radiosondes into the atmosphere to get the true values of potential temperature and mixing ratio in three different areas of study across the United States (Narragansett, RI, Huntsville, AL, and Houston, TX). The results from this study noted that by using an improved land-use dataset with finer resolution in WRF, a better representation of coastlines and fields of vegetation parameters was offered, along with improved predictions of boundary layer profiles.

It was described in [27] how the complexity of the land (terrain, land use, and soil) around DPG leads to the evolution of several well-observed mesoscale flow systems along with discussing how the DPG mesoscale playa breeze could be masked by interactions with other competing local mesoscale circulations. It was found that the local topography could induce circulations stronger and of greater extent than the playa breeze. The study of [14] noted that WRF forecasts were underpredicting the nocturnal cooling over the sparsely vegetated silt loam soil areas around Dugway Valley, and it was found that significant errors were introduced from both the improper initialization of soil moisture and in the parameterization of soil thermal conductivity for silt loam and sandy loam soil texture types. The result of their model simulations showed a mean positive bias error (3.4 °C) in 2 m AGL temperature forecasts across the early morning hours. It was revealed through additional simulations that these temperature errors were sensitive to the soil thermal conductivity parameterizations used in the land surface option they selected for WRF, which controlled the ground-heat flux. In fact, a different parameterization substituted for soil thermal conductivity reduced these biases significantly [27]. It was found by [28] that improvements to the model parameterization of PBL turbulence and surface layer exchange during conditions of stable stratification could significantly improve nighttime simulations of temperature and wind structures during MATERHORN.

1.3. Study Goals

The aim of this study was to use the WRF model to simulate diurnal flows across DPG throughout the full duration of the MATERHORN IOP6, which spanned the period of 2012 0800 UTC Oct 14–0800 UTC Oct 15. Our focus was upon the katabatic/anabatic, valley, and playa wind systems of the area. We were interested in how different WRF configuration setups such as choice of large-scale meteorological input, land surface soil thermal conductivity formulation method, and choice of boundary layer turbulence and radiation physics parameterization might alter these local flows and the diurnal temperature differences between the GSL playa and the sagebrush area of the Dugway Valley (just east of Granite Peak). We also wanted to explore if there was a reasonable possibility that lower-tropospheric weak-synoptic forcing early in IOP6 was still enough to exert some influence at the surface, particularly on how the flow evolved over the GSL playa and over the Dugway Valley. The goal was to assess by using a limited number of model setup members (i) which of our anticipated forcing effects seemed to have the greatest impact on local mesoscale flows during IOP6 and (ii) would IOP6 serve well as a case study period for future work focused on testing different mesoscale-to-LES nesting strategies using WRF.

Although airborne lidar and radiosonde measurements during 14 October did show a modest late-afternoon convective boundary layer of up to 2200 m ASL, the surface-sensible heat flux was also considerably lower on this day than for the last few previous October IOPs [29]. This was potentially due to the lingering effects of a rain event from a few days prior. This characteristic of IOP6 is what persuaded us to focus on a pair of 1.5 order turbulence kinetic energy (TKE) local schemes, which are generally expected to perform better at night under stable conditions when we anticipated interesting flows around Granite Peak and the Dugway Valley. For example, in previous MATERHORN research [28] it was found that a local scheme performed best at the sub-kilometer grid spacing for the surface and lower boundary layer fields. In general, at typical mesoscale resolutions non-local PBL schemes in WRF tend to perform better under convectively unstable daytime conditions with deeper boundary layer depth (larger turbulent eddies), while at night under stable conditions with more shallow boundary layers the local schemes tend to do better. However, surface and boundary-layer biases in model parameters are not always universal across all local and non-local schemes for all geographical and meteorological regimes [30–33]. In general, it has been found that non-local schemes such as the Yonsei State University parameterization [34] tend to handle vigorous deep mixing and entrainment better in convectively unstable conditions, but that under conditions of stable stratification that local schemes perform better. In terms of model biases at the

surface (2 m AGL and 10 m AGL levels), biases can vary based on season, meteorological conditions, geographic location, and other considerations. It is quite likely that such surface level model biases are a mix of contributions of errors from initial conditions, surface state, model resolution, boundary layer and surface layer parameterization, and land surface treatment [35].

At sub-kilometer grid spacing (turbulence gray area), there is rarely consensus regarding which approach is better, and this is largely because each scheme becomes more dependent upon grid scale and how well the resolvable and non-resolvable transport contributions are partitioned. Each scheme may have a particular grid scale where this is handled better. New approaches such as those developed by [30] attempt to modify an existing mesoscale turbulence scheme so as to make it "scale aware". This has been found to have some success [36]. Another option for sub-kilometer grid spacing is to go with a 3D-explicit large-eddy simulation (LES) approach available in WRF, which also is a bit in the gray area at such scales. Generally, for unstable regimes the grid spacing range between 250 m and 500 m is probably handled better using LES, but at night under stable conditions a traditional mesoscale PBL scheme may still be appropriate since even the largest turbulent eddies are very small. Scale-aware schemes such as [30] are also an option at this range. We chose to compare a couple of the local PBL turbulence options (along with their preferred surface-layer-scheme option) available in WRF for our 0.452 km nest (discussed in next section), and our decision was based on (i) interest in mesoscale flows across the Dugway Valley and near/around the Granite Peak at night under stable conditions, and (ii) the lack of a really deep convective PBL depth observed during the day. By using a local PBL scheme throughout the entire simulation (spanning both day and night hours) at 0.452 km grid spacing, we felt we could perform well during the stable regime while not significantly degrading during the day so as to impact the results focused on the playa breeze circulation. Using an LES was considered for this nest, but there was concern that at 0.452 km it was still too coarse for the use of LES during the nighttime stable regime hours. This is something we can further explore in future work. Another option could have been to run the day and night simulations separately using a different PBL treatment for each; however, we preferred examining across a single simulation period for this work so that initial spin-up concerns could be alleviated.

2. Materials and Methods

All WRF simulations applied telescopic nesting with a 0.452 km horizontal grid spacing innermost nest and used 90 terrain-following vertical levels (model top of 50 hPa). The relatively high vertical resolution was used to compliment the use of sub-kilometer horizontal resolution, ensuring that vertical grid spacing did not become comparable to or even larger than horizontal grid spacing which can generate numerical issues in WRF [37]. All simulations spanned the period from 00 UTC 14 Oct–08 UTC 15 Oct 2012. There was no data assimilation applied, so the first 8 h were allowed for model spin up. Output generated using the model was compared to data collected using the DPG Surface Atmospheric Measurement Systems (SAMS) sites, in addition to special meteorological observations provided courtesy of the MATERHORN field campaign [38]. Each of the DPG SAMS sites (Figure 1) record winds at a temporal and spatial resolution appropriate for resolving features of a few kilometers in scale, although a special mini-SAMS network of stations was set up in Dugway Valley east of Granite Peak during MATERHORN and allowed for sub-kilometer resolution [39]. A total of five WRF setups were performed for comparison, with each using a slightly different configuration of input and/or runtime options.
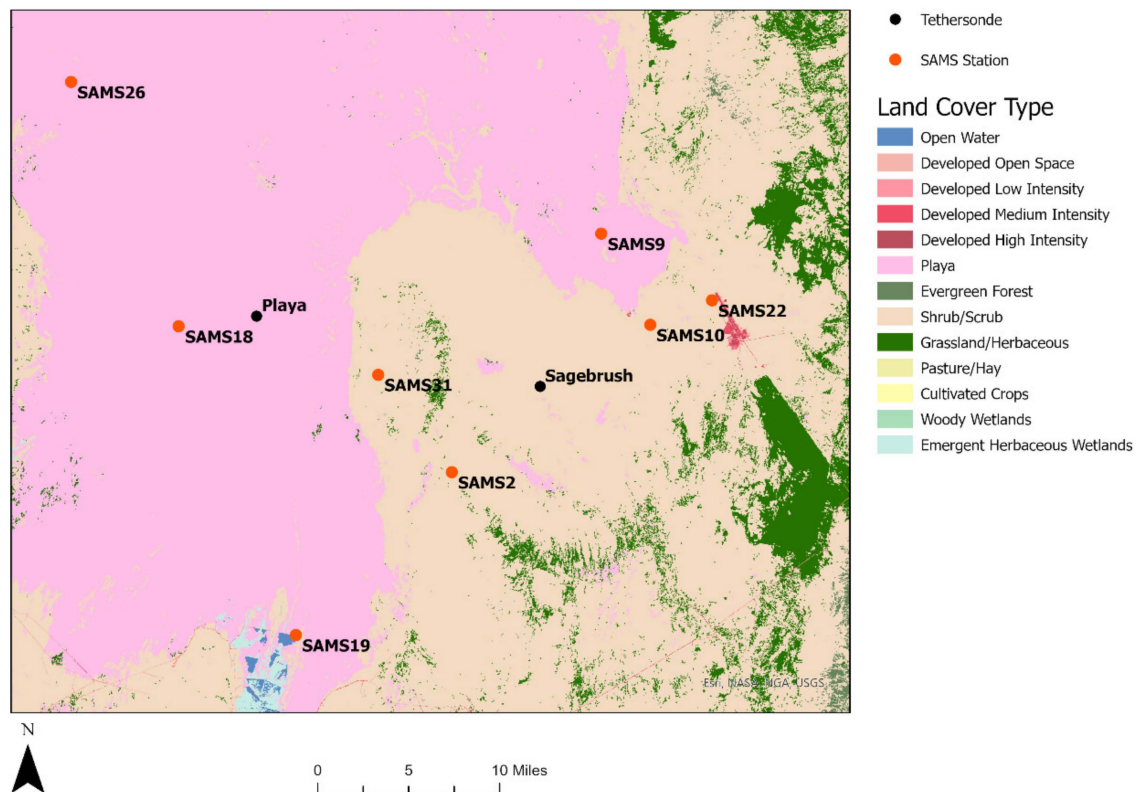
SAMS and Tethersonde Locations

Figure 1. DPG land use with SAMS and MATERHORN tethersonde sites, along with NLCD high resolution land-cover categories.

The full hierarchy of nests employed were 12.200 km, 4.067 km, 1.356 km, and 0.452 km (spatial and time-step nesting ratio of 3:1). The large-scale model advective time step (used for nest 1) was 27 s. The dimensions of these nests, respectively, were 205×205, 175×175, 133×133, and 169×169. Model setup 1 (MS1) used the Mellor–Yamada–Janjic (MYJ) [40] local parameterization scheme for PBL turbulence, Monin–Obukhov [41] formulation for the surface layer, Noah [42–44] for the land surface, Dudhia [45] for 1D-column treatment of shortwave radiation (with slope and shading effect options [46]), Rapid Radiative Transfer Model (RRTM) [47] for long wave radiation, Thompson scheme [48] for microphysics, Kain–Fritsch [49] for deep convection (outermost grid only), a Cartesian-level- based treatment for the 2D Smagorinsky horizontal turbulent diffusion [50], the 3rd and 5th order advection options, the 6th order numerical diffusion filter [51] option, and a higher value (0.5) for the name list "epssm" coefficient to control slope-generated instabilities due to vertically propagating sound waves [52]. The setup MS1 also used the NCEP NAM model [53] output for initial and lateral boundary conditions, as well as the default WRF USGS [54] land-use (24 category, 30 arc sec resolution) and STATSGO [55] soil-texture (16 category, 30 arc sec resolution) datasets.

The remaining model setups (MS2, MS3, MS4 and MS5) all used a higher resolution and categorical land use based upon the NLCD 2006 40-category [56] dataset remapped to USGS categories (27 categories including three added using NCAR over CONUS for playa, white sand, and lava 1 arc-sec resolution) and a 19 category NCAR-modified version of STATSGO soil-texture dataset (playa, white sand, and lava added over CONUS). These three additional categories can be important when performing sub-kilometer mesoscale modeling in certain regions of the western United States, such as DPG. The land use and soil-texture classifications for the 0.452 km nest domain (for both default and higher classification/resolution datasets) are shown in Figure 2a-d. The higher resolution 3 arc

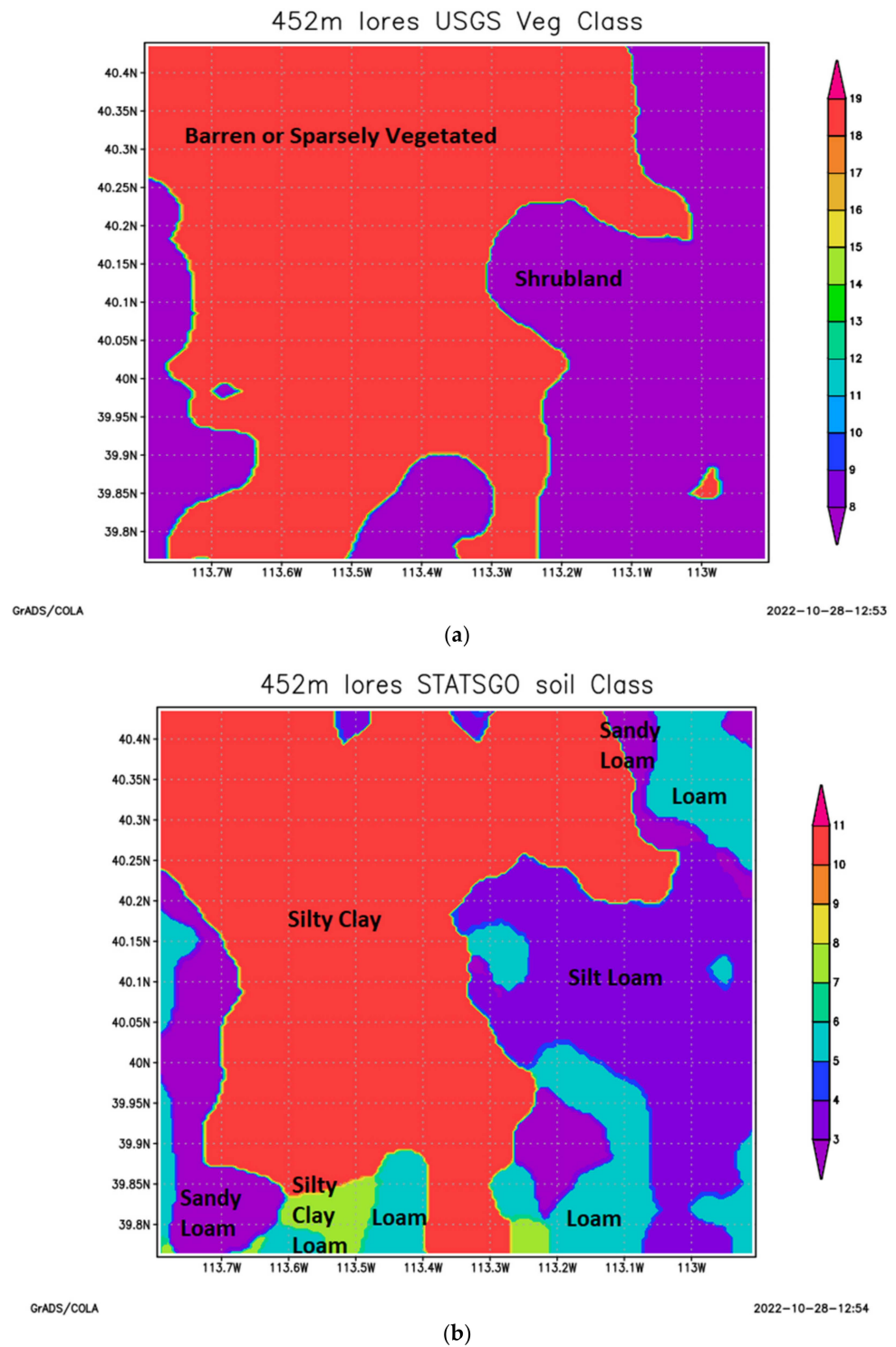sec Shuttle Radar Topography Mission (SRTM) terrain database was also used [57] for this study and for all the setups.

(**a**)

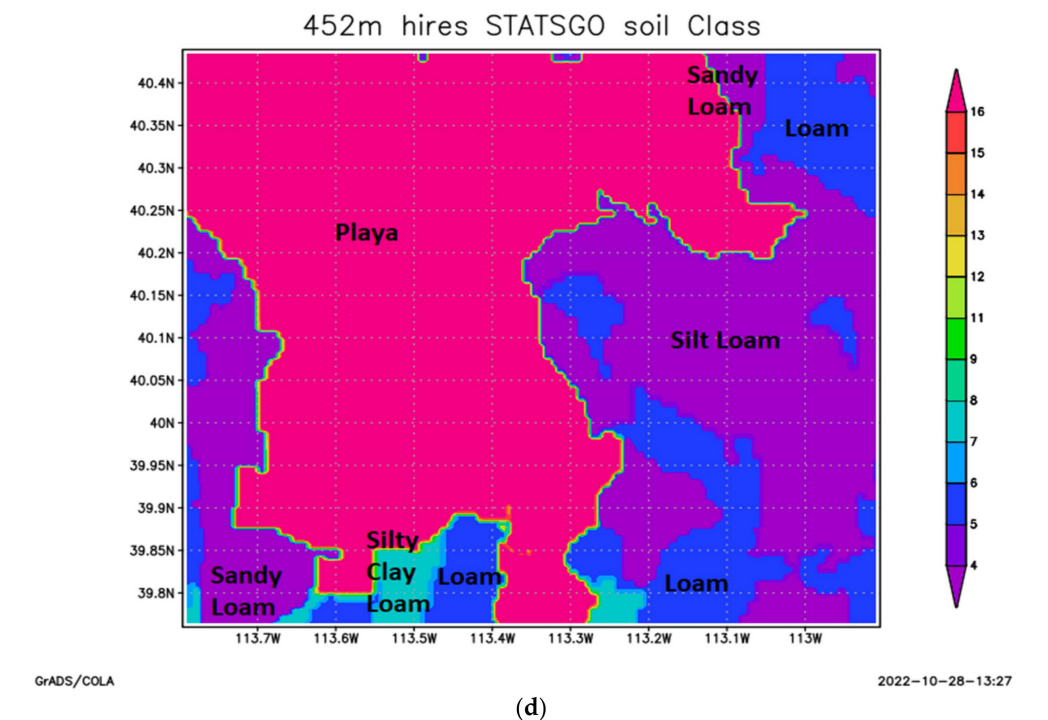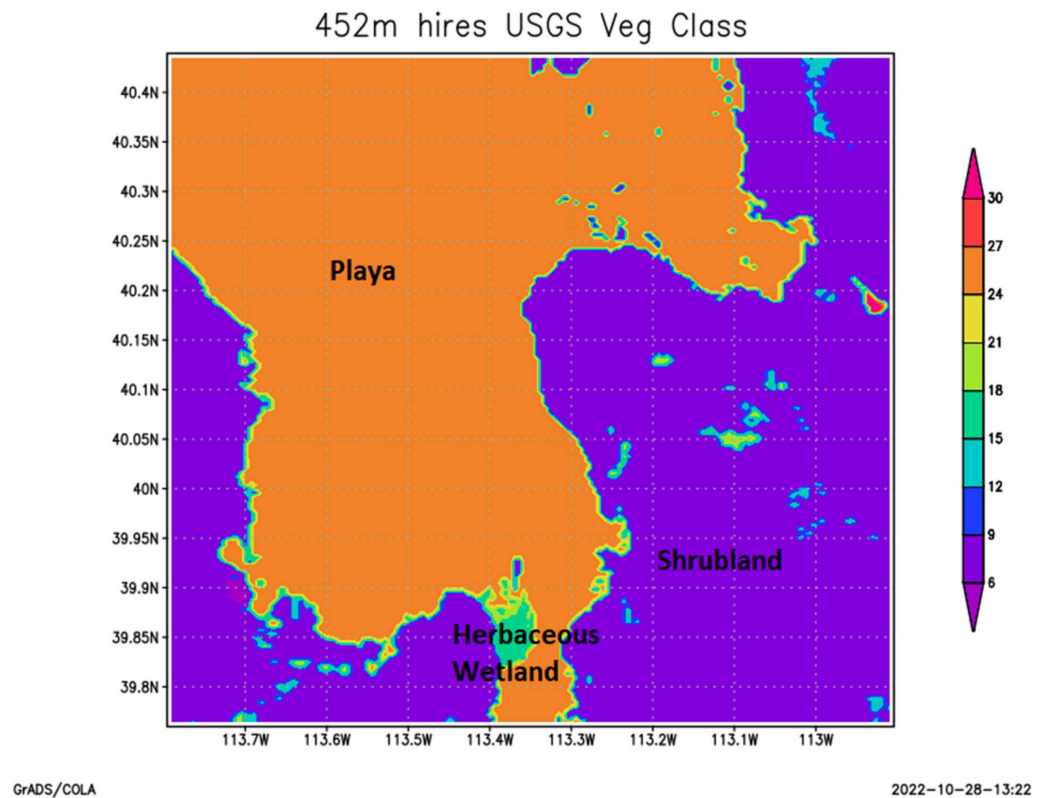(**b**)

Figure 2. *Cont.*

(c)

(d)

Figure 2. (**a**) Lower resolution land use/vegetation classes used for MS1 for the 452 m grid-spacing inner nest. (**b**) Lower category STATSGO soil-texture classes used for MS1 for the 452 m grid-spacing inner nest. (**c**) Higher resolution land use/vegetation classes used for MS1 for the 452 m grid-spacing inner nest. (**d**) Higher category STATSGO soil-texture classes used for MS1 for the 452 m grid-spacing inner nest.

The MS2 also differed from MS1 in that it used GFS $\frac{1}{2}$ degree model [58] output. Both GFS and NAM 00 UTC 14 October 2012 cycles were used. The MS3 only differed from the MS1 through use of the higher resolution/category land-use and soil-texture datasets. The MS4 differed from the MS1 in that it used the Quasi-Normal Scale Elimination (QNSE) options for turbulence (which are a local parameterization scheme for PBL along with a surface layer scheme) [59], horizontal turbulence diffusion using Cartesian versus model level surfaces [50], Goddard options for both shortwave [60] and longwave [61] radiation, GFS $\frac{1}{2}$ degree model output, and the McCumber and Pielke [62] soil thermal conductivity parameterization rather than the default [63] option in the Noah land surface. The MS5 differed from the MS4 only in that it used NAM rather than GFS $\frac{1}{2}$ degree model output. These variants of the setups are summarized in Table 1.

Table 1. Datasets and parameterization schemes used for each model setup performed in this study. The NLCD 2006 40 land-use categories were remapped to the original 24 USGS categories with three additional added using NCAR for playa, white sand, and lava over CONUS. For soil texture, NCAR also added playa, white sand, and lava categories over CONUS.

	MS1	MS2	MS3	MS4	MS5
Land Use and Soil Texture	USGS GTOPO30 (30 arc sec; 24 categories) and STATSGO 30 arc sec with 16 soil categories (no playa)	NLCD 2006 (1 arc sec; 27 categories) and STATSGO 30 arc sec with 19 soil categories (includes playa)	NLCD 2006 (1 arc sec; 27 categories) and STATSGO 30 arc sec with 19 soil categories (includes playa)	NLCD 2006 (1 arc sec; 27 categories) and STATSGO 30 arc sec with 19 soil categories (includes playa)	NLCD 2006 (1 arc sec; 27 categories) and STATSGO 30 arc sec with 19 soil categories (includes playa)
Boundary-Layer Physics	MYJ	MYJ	MYJ	QNSE	QNSE
Initial/Lateral Boundary Conditions	NAM 12- -km from NCEP	GFS $\frac{1}{2}$ degree from NCEP	NAM 12- -km from NCEP	GFS $\frac{1}{2}$ degree model NCEP	NAM 12- -km from NCEP
Turbulent Diffusion	Horizontal diffusion on terrain following surfaces	Horizontal diffusion on terrain following surfaces	Horizontal diffusion on terrain following surfaces	Horizontal diffusion on Cartesian z-following surfaces	Horizontal diffusion on Cartesian z-following surfaces
Radiation	Dudhia option for shortwave and RRTM for long wave	Dudhia option for shortwave and RRTM for long wave	Dudhia option for shortwave and RRTM for long wave	Goddard options for short wave and long wave	Goddard options for short wave and long wave
Thermal Soil Conductivity Over Sandy and Silt Loam Soil Types	Existing parameterization in Noah land-surface model	Existing parameterization in Noah land-surface model	Existing parameterization in Noah land-surface model	New parameterization in Noah land-surface model	New parameterization in Noah land-surface model

Previous WRF studies by [27] indicated that improved soil-moisture initial conditions and a modified parameterization of soil thermal conductivity in the Noah land surface model were effective in improving the model's ability to accurately predict near-surface temperatures (particularly during the nocturnal hours). This is the reason that some of the setups used the soil thermal conductivity parameterization of [63] with Noah. The initial soil-moisture fields for all setups were produced from either the GFS $\frac{1}{2}$ degree or NAM forecasts—so relatively coarse resolution input. The WRF model setups were executed for an area centered near Granite Peak (40.1 deg N, −113.35 deg W) within DPG.

3. Results

3.1. IOP6 Meteorological Conditions

Features of focus in the discussions that follow are shown in Figure 3 with the WRF modeling domain shown in Figure 4, and with the synoptic conditions spanning the IOP6 captured in Figure 5a–d. In Figure 5a–d, shown are four 700 hPa analyses (geopotential height, temperature, wind) for 0000 UTC 14 October, 1200 UTC 14 October, 0000 UTC 15 October, and 1200 UTC 15 October. The most significant feature is a strong short-wave trough that ejects from western Kansas to the upper peninsula of Michigan throughout the period. Behind this exiting trough, ridging builds over the Intermountain West and into the study region. As mentioned previously, the IOP6 was defined as "quiescent" within the context of the MATERHORN definition [38,64], due to the mean lower tropospheric flow (such as at 850 hPa and 700 hPa) staying at or below 5 m/s within the duration of the study period.

Figure 3. Notable features referred to in the paper.

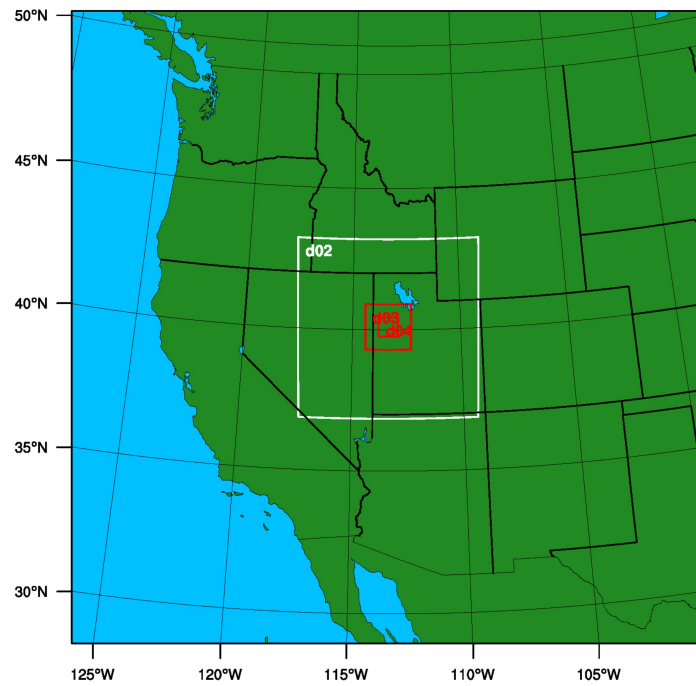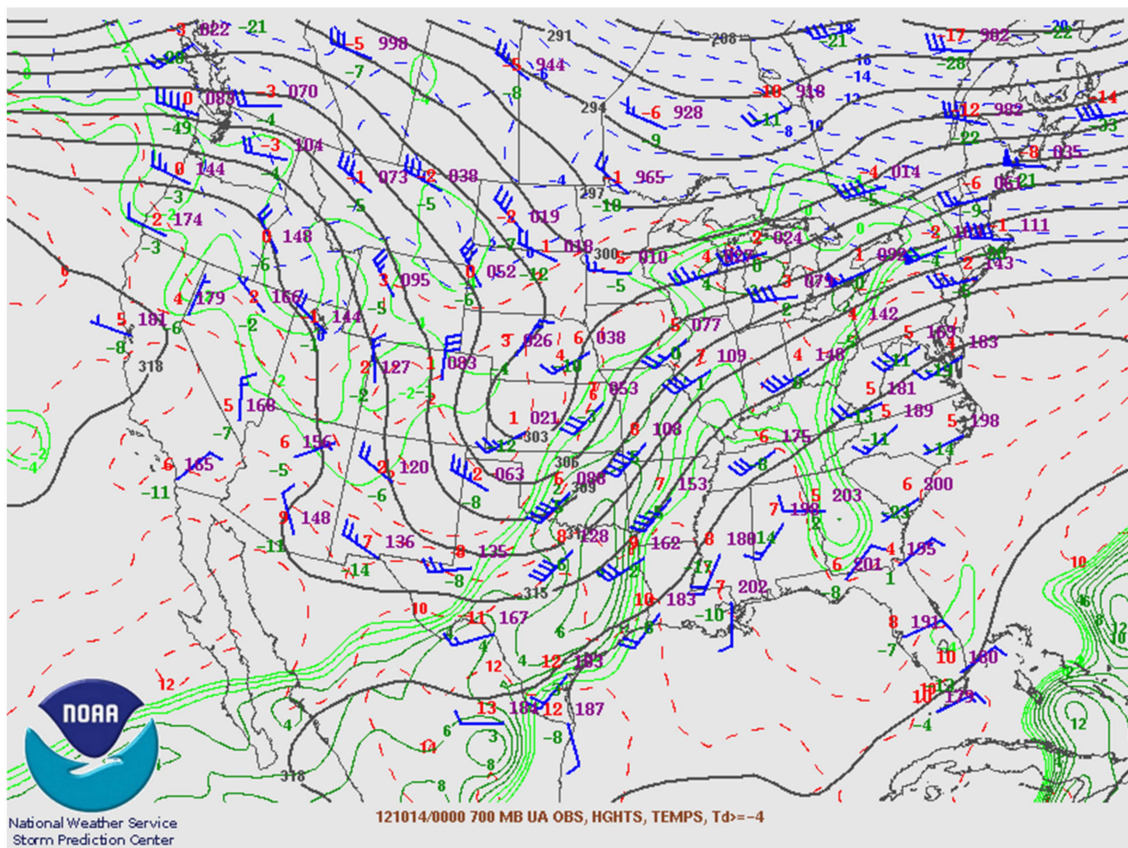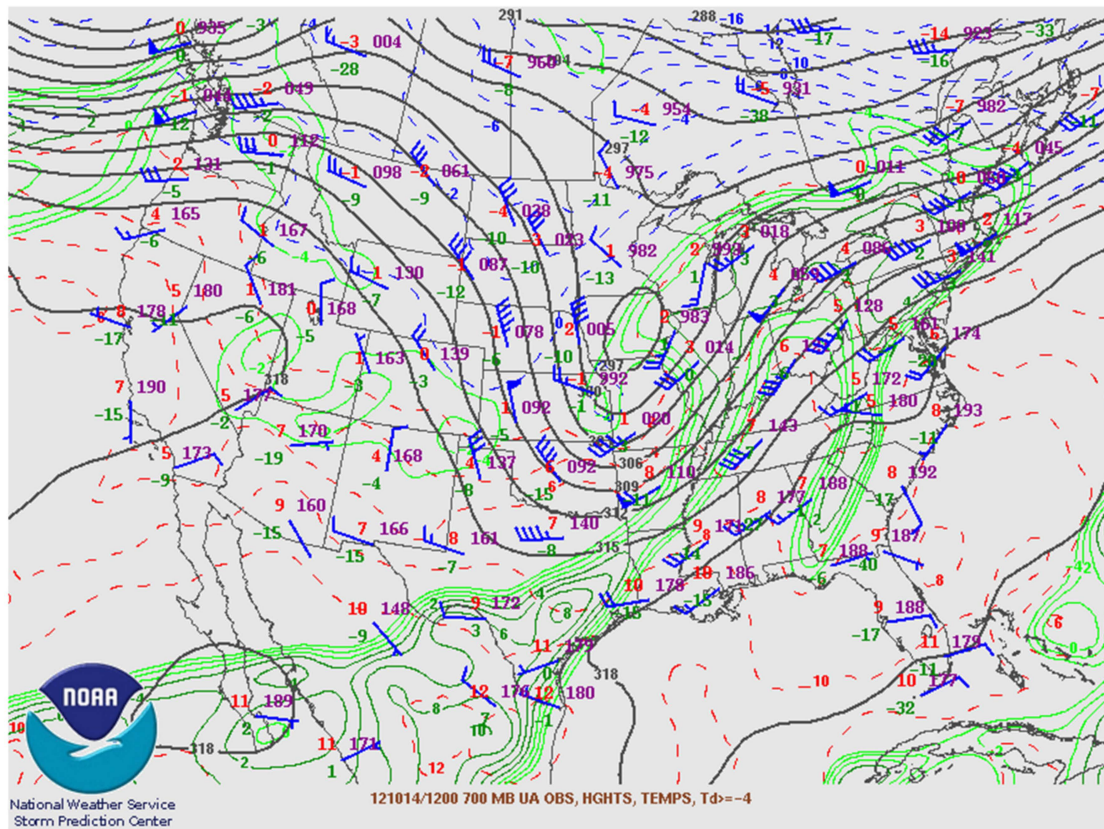**Figure 4.** WRF nest domains centered on DPG.

(a)

Figure 5. *Cont.*

121014/1200 700 MB UA OBS, HGHTS, TEMPS, Td>=−4

(**b**)

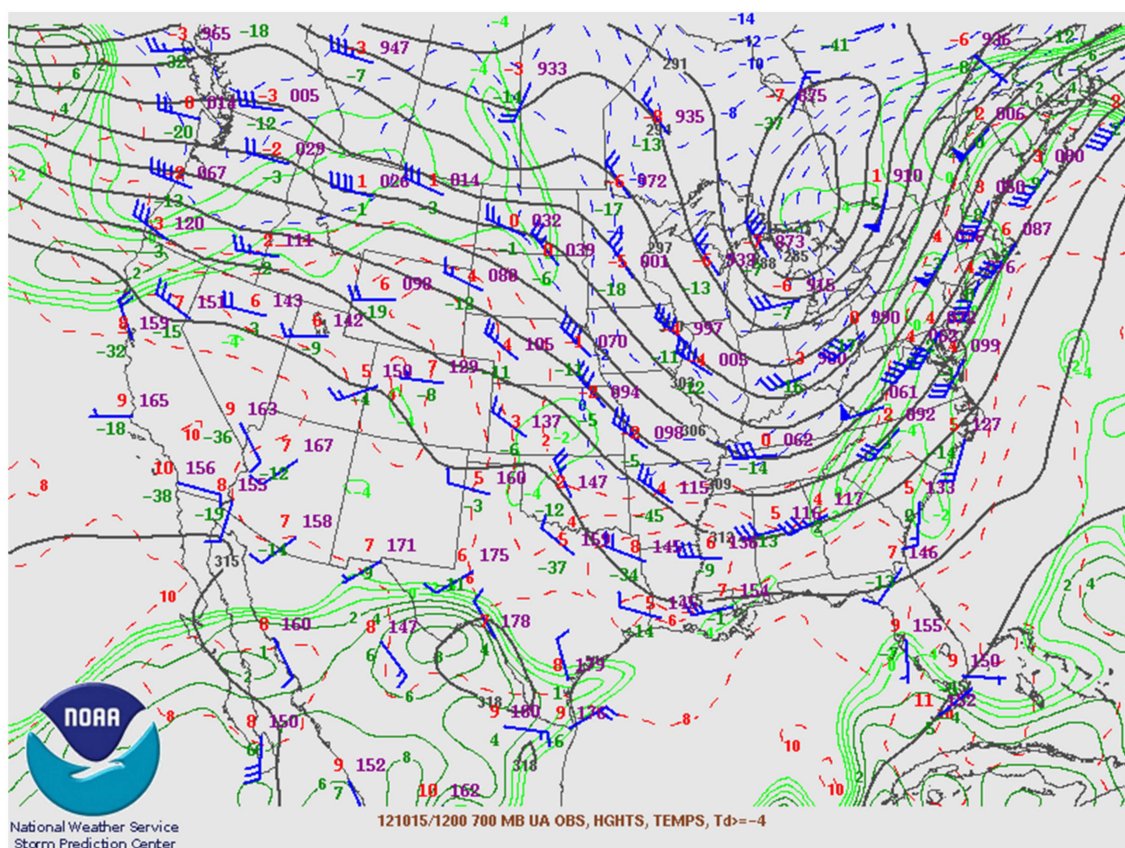121015/0000 700 MB UA OBS, HGHTS, TEMPS, Td>=−4

(**c**)

Figure 5. *Cont.*

(**d**)

Figure 5. (**a**) Upper-level 700 hPa analysis charts for 10-14-0000 UTC. (**b**) Upper-level 700 hPa analysis charts for 10-14-1200 UTC. (**c**) Upper-level 700 hPa analysis charts for 10-15-0000 UTC. (**d**) Upper-level 700 hPa analysis charts for 10-15-1200 UTC. Graphics from NOAA.

However, the NAM (as well as GFS) forecasts for the period 0000 UTC 14 Oct–1200 UTC 14 Oct may have predicted slightly greater northwesterly flow at levels at or below about 800 hPa early in IOP6, which possibly impacted the evolution of local surface flows that night (early morning of 14 October) in the WRF (for example, in terms of the timing of the development of the Dugway Valley downvalley flow). In the findings discussed by [65], a mesoscale regional forcing known as the Great Basin Confluence Zone (GBCZ) is given for favoring southerly or northerly wind regimes over DPG, which can be opposite to the diurnal southerly or northerly flow direction favored by the local topography of the area (orientation of main valley systems being meridional).

Small model displacements of large-scale features in such a synoptic pattern (and the resultant placement of the main baroclinic zone either north or south of DPG) can lead to substantial errors in local flow. For example, this is discussed in [66]. For best capturing local flows and turbulence structure, it is necessary to accurately capture the timing and location of the larger-scale atmospheric disturbances. Ridging was firmly in control by the end of the IOP6 (early morning 15 October) with very weak southwesterly flow aloft, and the local flows became dominated mostly by the topographical and land use thermodynamics (the regional flow component appears more in line with the southerly Dugway Valley downvalley direction on the night/morning of the 15th). Another point to make about flow over the area is that both local and regional soil moisture initialization can impact the overall model solution (through biasing 2 m AGL temperature)- an initial reaction might be to think that only the local soil moisture initialization (via the inner model nest of the model) would have the greatest impact [67]. Since GFS or NAM soil moisture was used to initialize all the setups, we did not look directly at that impact in this paper.

Another aspect of IOP6 is that it followed a regional precipitation event a few days prior on 14 October 2012 [27,29]. It has been observed that playa surfaces tend to have lower surface albedo for several days after a rain event, along with changes in the crust, in the salinity, and in the soil moisture near the playa surface [68]. In [27] it was shown that after the rain event preceding 14 October 2012, the soil moisture observation at DPG gradually increased, while the GFS soil moisture responded suddenly and the NAM soil moisture had little response at all. The impacts of the precipitation on both observed and GFS soil moisture appeared to extend out several days. The MATERHORN study [67] shows that rainfall on the playa produces a short-term (1–3 day) decrease in surface albedo, decrease in Bowen ratio, increase in net radiation, increase in ground heat flux, increase in thermal soil conductivity, decrease in sensible heat flux, and increase in latent heat flux. Evapotranspiration follows with latent heat flux, and there appears to be an e-folding time of about 3 days [69]. However, after a few days post-rainfall, the sensible heat flux appears to return to values closer to those as before the event.

The observed diurnal temperature-range differences between the GSL Playa and nearby off-playa sagebrush regions appear to have been reduced throughout IOP6 [38], which offers some support to the idea that recent precipitation led to some short-term changes in the surface sensible and latent heat fluxes over each surface (even at 2 days post-event) along with their respective albedo values. The study of [70] found that more typically the mean afternoon temperatures over the sagebrush across two different MATERHORN campaigns (Fall 2012 and Spring 2013) tended to be a few degrees warmer than over the playa. In the spring, the soil moisture tended to be lower over the playa and higher over the sagebrush, while the albedo tended higher over the playa and lower over the sagebrush (versus the fall). In addition, [27] found that the diurnal temperature range over the sagebrush, averaged across two fall campaigns (2011 and 2012), was considerably higher than that of the playa (19.2 C vs. 13.8 C).

Figures 6 and 7 illustrate the variation of 2 m AGL surface temperature at several SAMS sites located both on the GSL Playa and off the playa throughout the duration of IOP6. These sites are also located on Figure 1. The observations show that off-playa sites generally have only a slightly higher amplitude of afternoon surface temperature than that of the playa sites during IOP6. However, on both nights throughout IOP6, the observed minimum temperature trends several degrees cooler off-playa over the sagebrush versus on the playa. Overall, the IOP6 diurnal range of temperature between off-playa and playa sites appears less than what was typically observed throughout the MATERHORN Fall 2012 campaign, and this could again be due to the lingering impact of the precipitation event on 12 October. The late night and early morning hours of 14 October also appear to have been a few degrees cooler at most sites, perhaps due to synoptic differences.

Figures 8a–d and 9a–d show the evolution of the wind speed, and Figures 10 and 11 wind direction, at the same SAMS sites. There are indications of a short-lived flow reversal to off-playa direction at some sites (such as sites 10 and 22) during the late afternoon hours of 14 October, which is suggestive of a weak and poorly established playa breeze along the eastern boundaries of the GSL Playa. The winds along the eastern periphery of the GSL Playa at most sites were typically on-playa (flow out of east-to-southeast) through much of IOP6. The mean wind speeds throughout IOP6 at all SAMS sites were relatively low and rarely in exceedance of 5 m/s. In addition, Figures 8a–d and 9a–d show that each site experienced regular periods of rises and dips in wind speed, which seem suggestive of smaller-scale sub-diurnal features throughout the IOP6, although a more careful examination of filtered versus raw observations is necessary to really address the full nature of these [71]. Here, we are comparing just the instantaneous values of model output and observations at the top of each hour to produce gross comparisons through IOP6.
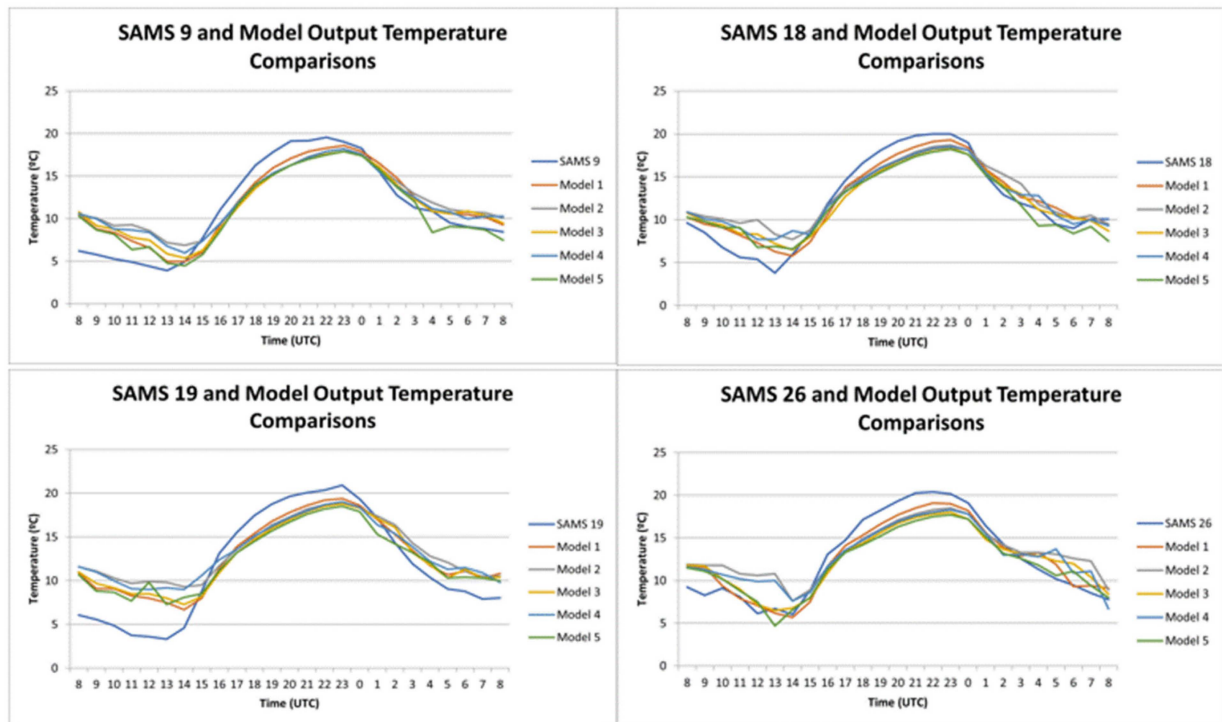
Figure 6. Observed 2 m AGL surface temperature (°C) compared with model simulated 2 m AGL surface temperature (°C) for the different experiments MS1 through MS5 across IOP6 at several different SAMS playa sites as shown in Figure 1.
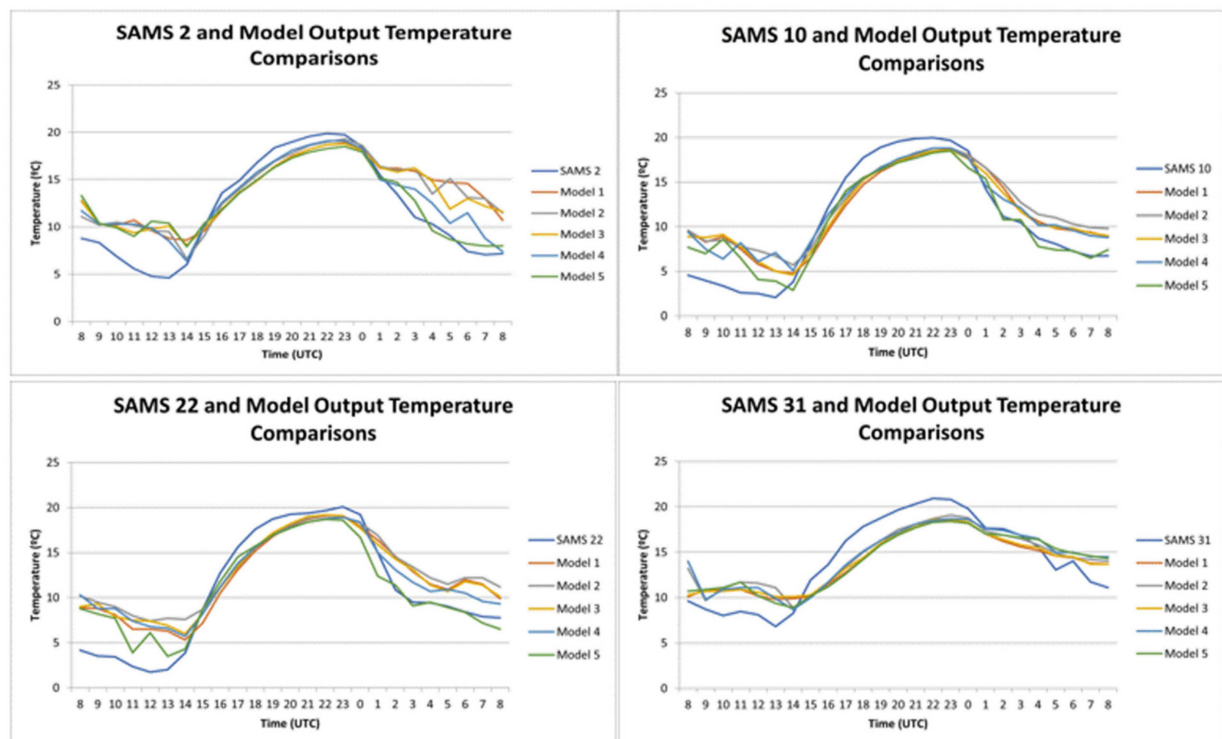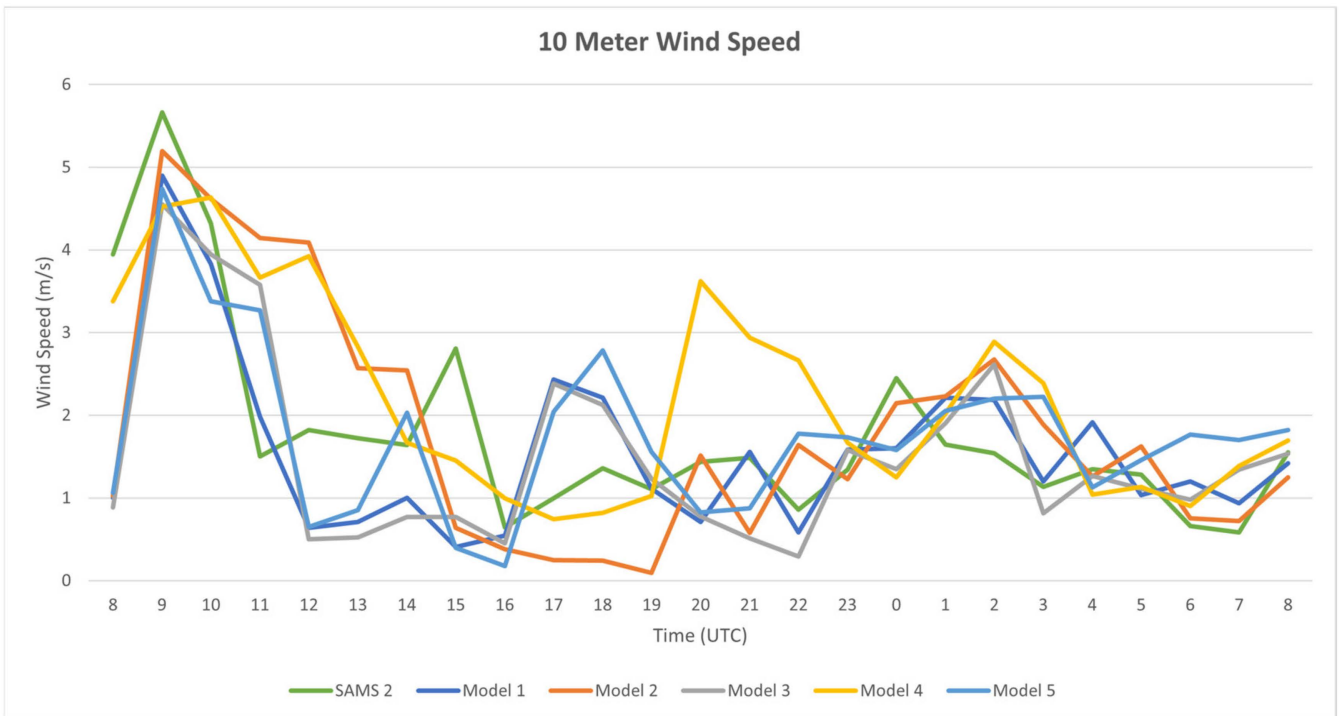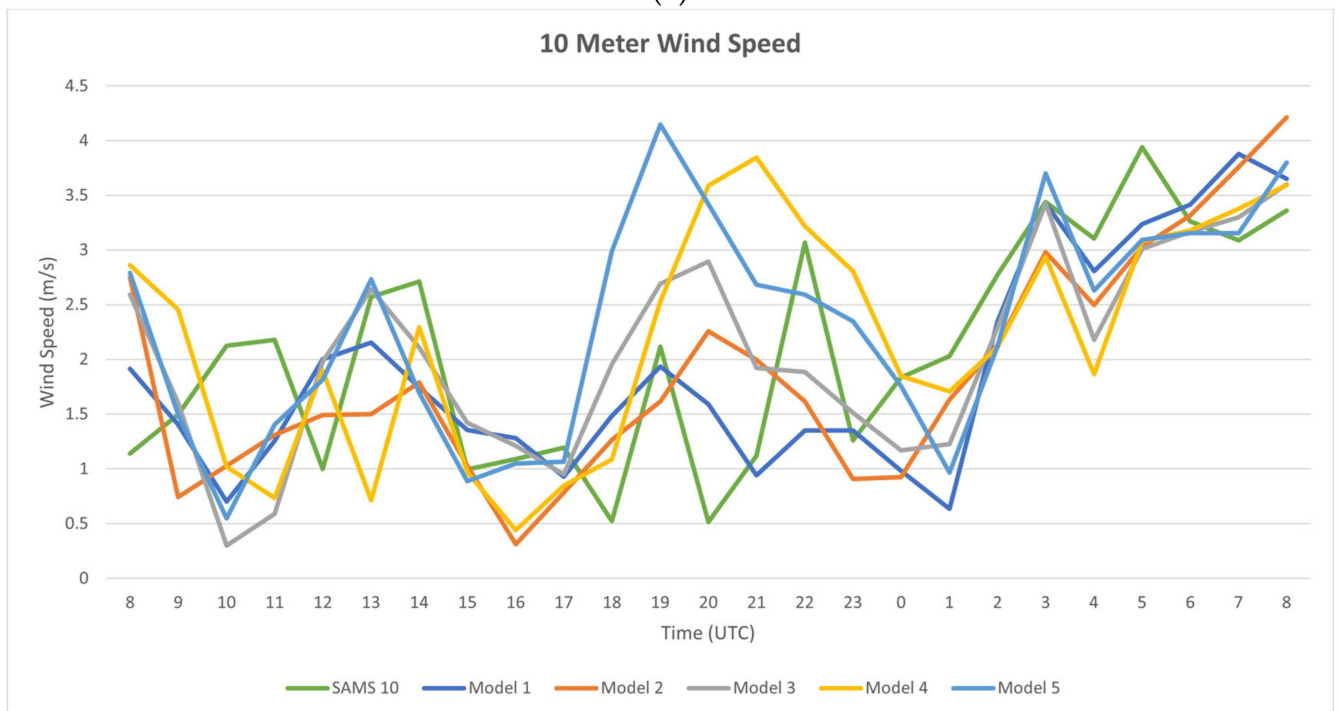

Figure 7. Observed 2 m AGL surface temperature (°C) compared with model-simulated 2 m AGL surface temperature (°C) for the different experiments MS1 through MS5 across IOP6 at several different SAMS off-playa sites as shown in Figure 1.
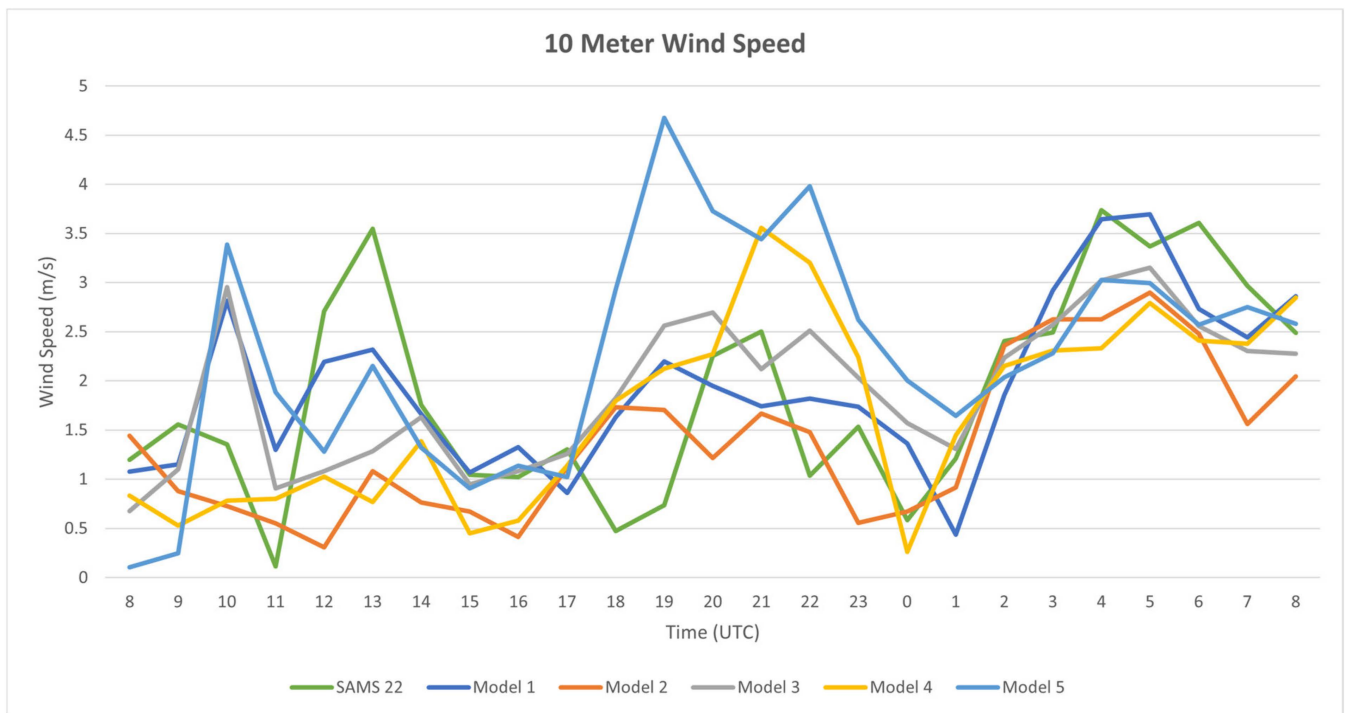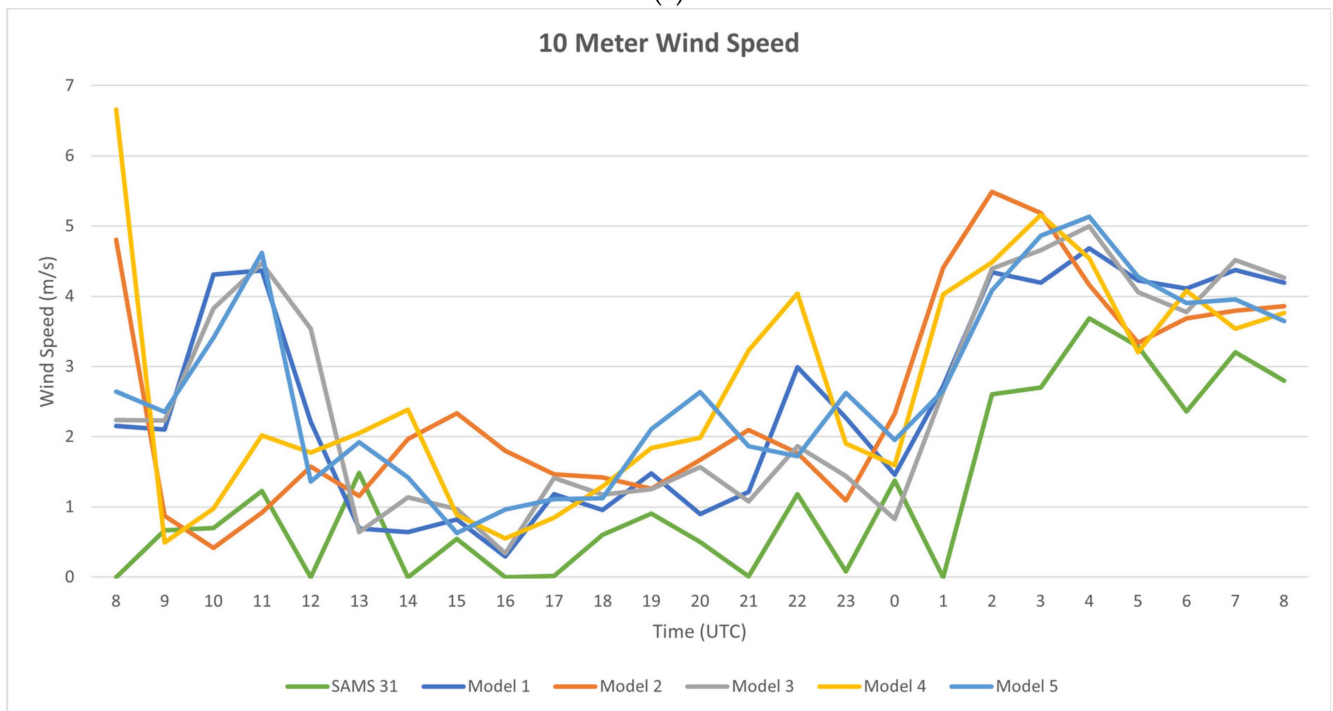
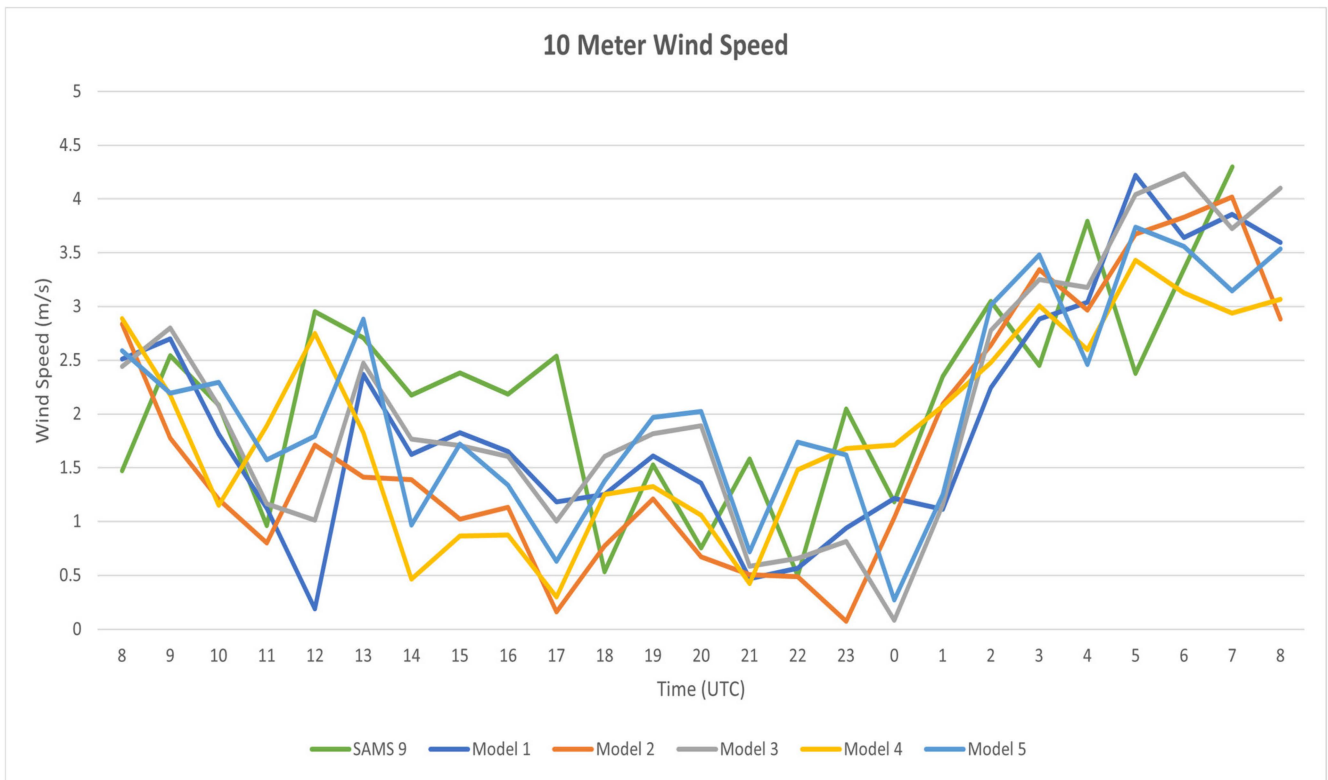(**a**)

(**b**)

Figure 8. *Cont.*

(**c**)

(**d**)

Figure 8. Observed 10 m AGL surface wind speed (m/s) compared with model-simulated 10 m AGL surface wind speed (m/s) for the different experiments across IOP6 at SAMS off-playa (**a**) site 2, (**b**) site 10, (**c**) site 22, (**d**) site 31 as shown in Figure 1.

(**a**)

(**b**)

Figure 9. *Cont.*

(**c**)

(**d**)

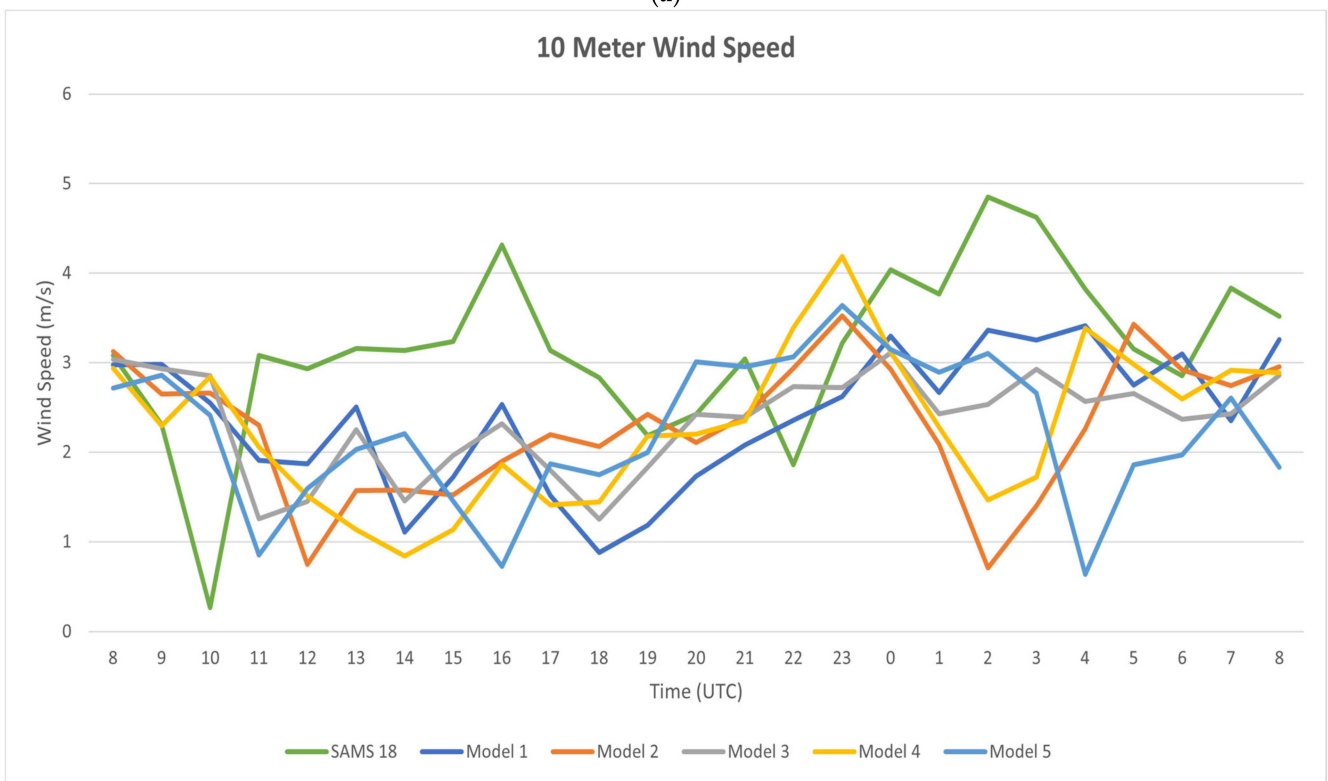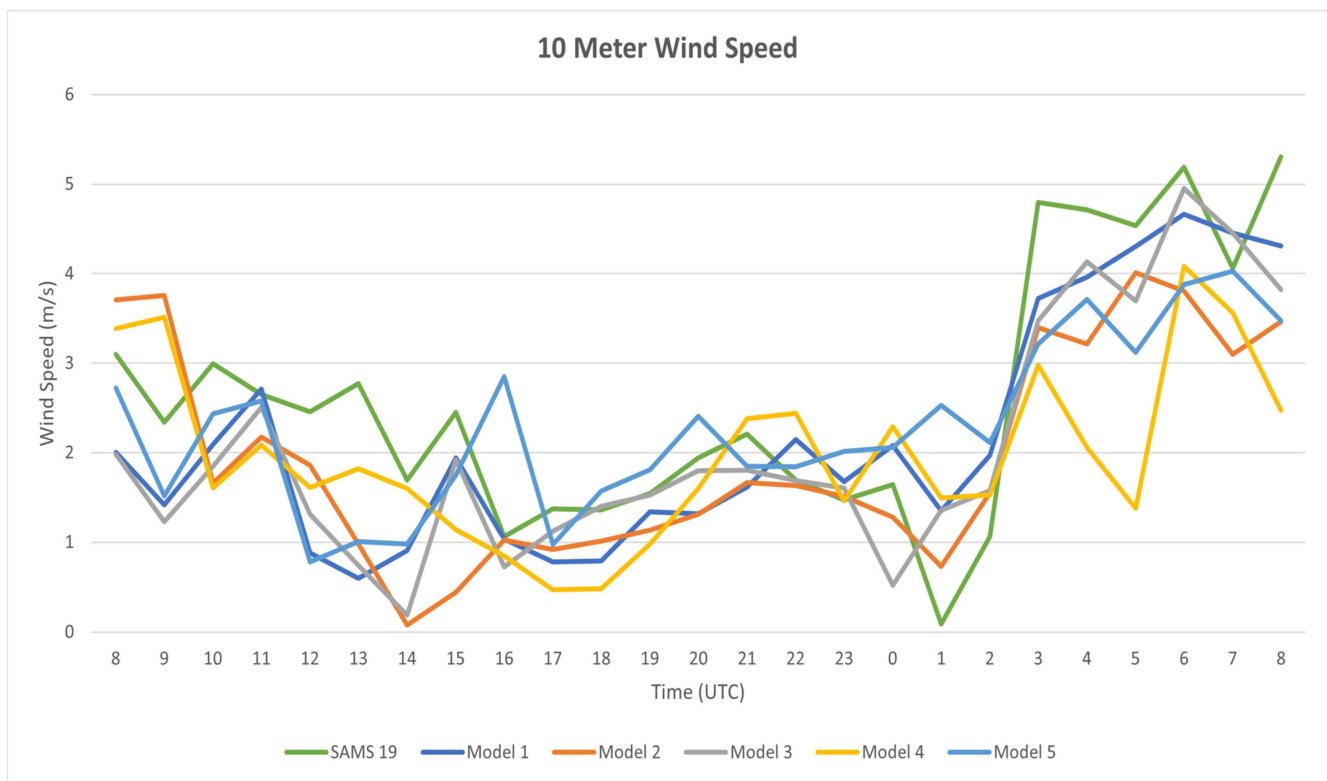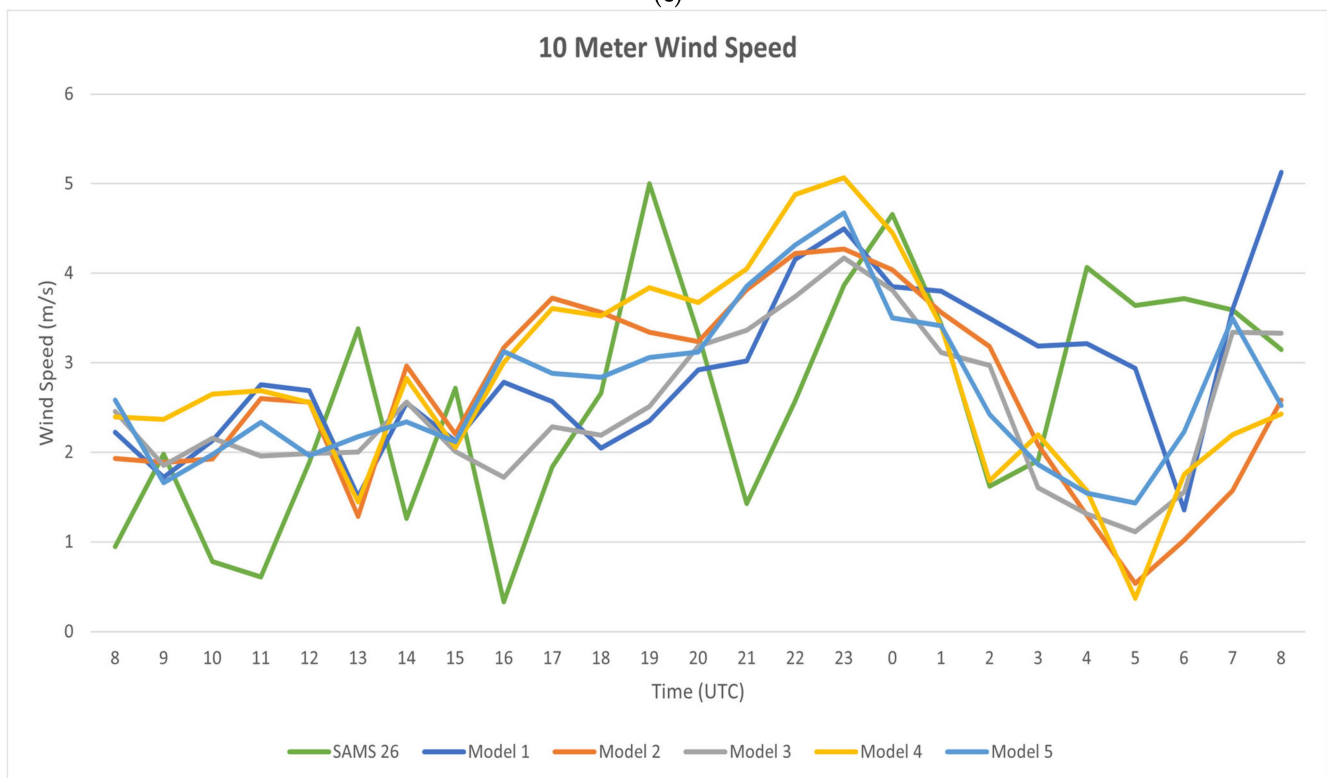**Figure 9.** (**a**) Observed 10 m AGL surface wind speed (m/s) compared with model-simulated 10 m AGL surface wind speed (m/s) for the different experiments across IOP6 at SAMS playa (**a**) site 9, (**b**) site 18, (**c**) site 19, (**d**) site 26 as shown in Figure 1.

Figure 10. Observed 10 m AGL surface wind direction (°) compared with model-simulated 10 m AGL surface wind direction (°) for the different experiments across IOP6 at several different SAMS playa sites as shown in Figure 1. From top left to bottom right: Sites 9, 18, 19, and 26.

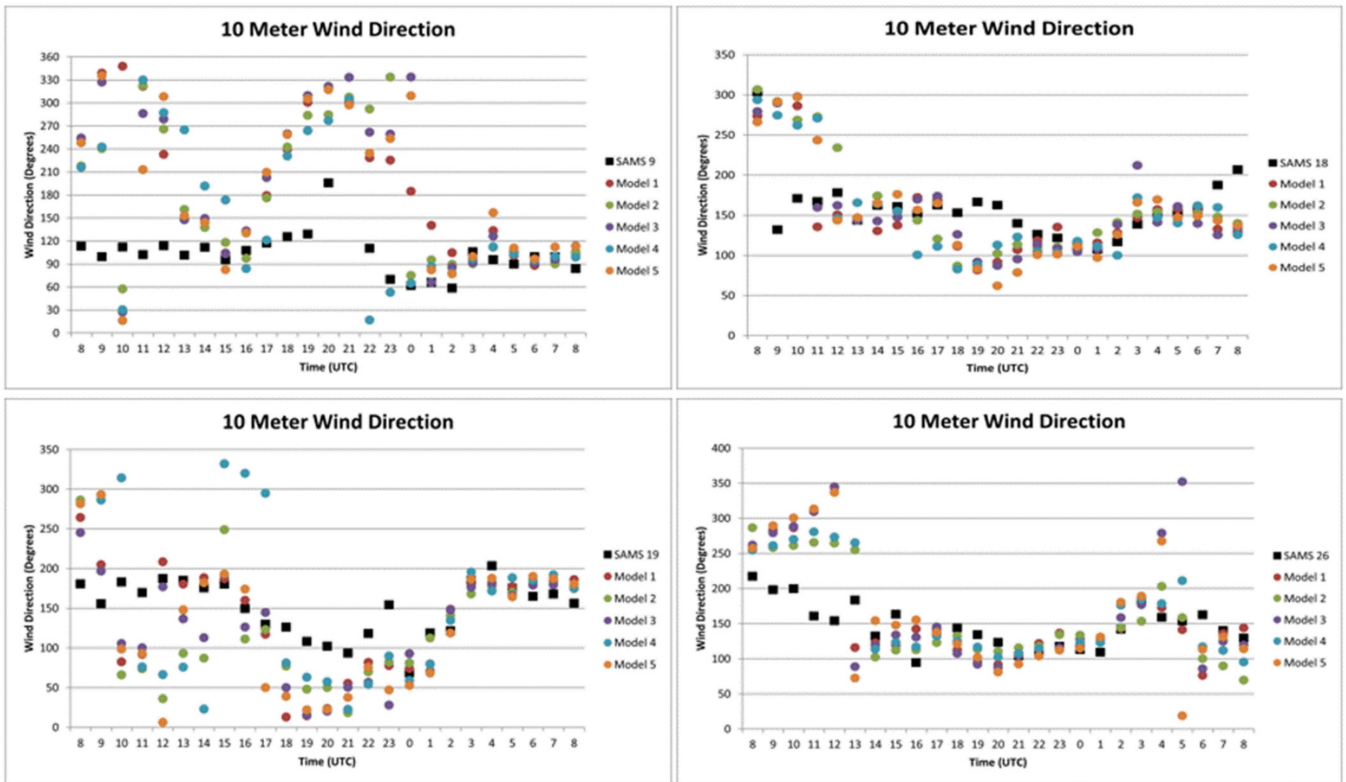**Figure 11.** Observed 10 m AGL surface wind direction (°) compared with model-simulated 10 m AGL surface wind direction (°) for the different experiments across IOP6 at several different SAMS off-playa sites shown in Figure 1. Top left to bottom right: Sites 2, 10, 22, and 31.
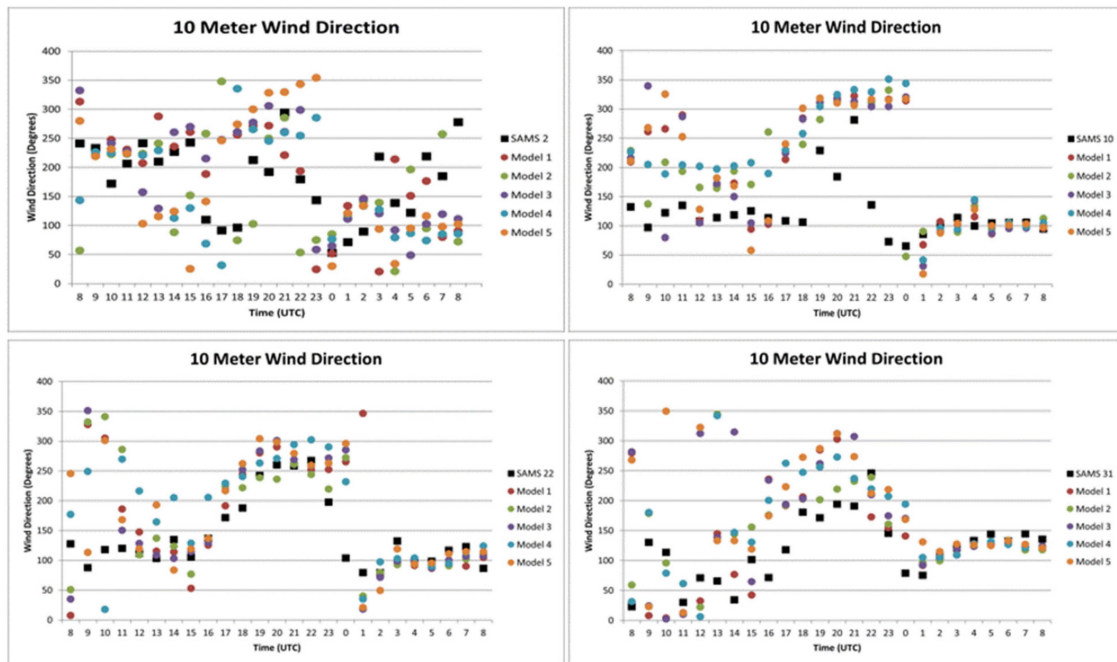
Several publications discuss the extreme complexity of the region as related to topography and land-use heterogeneity [64,72–76]. The mountains that surround this region of study, along with the overall smaller (than typical) temperature gradient between playa and off-playa locations, made it difficult to determine whether local wind patterns were being influenced significantly by playa-driven land surface temperature gradients, as opposed to more induced by the slopes of neighboring mountains (thermodynamically driven anabatic and katabatic flows). Additionally, although synoptic influence was weak, it was not completely absent. Therefore, geostrophic along with perhaps some other dynamic forcing due to topography [14] may have also exerted a small contributory effect.

Radiosonde, wind profiler, or aircraft data can sometimes detect evidence of a return circulation aloft within a well-developed direct circulation system such as a sea breeze [77] while under weak synoptic forcing. However, for playa breezes most evidence of a return flow is provided from simulations, if at all. Nevertheless, evidence of ascending/descending branches of the playa circulation (and possible return flow) is sometimes captured in simulations [51]. Strategically sited pilot balloons used by [25] did show some hints of very weak playa-breeze return flow aloft, but it was not overwhelming. In this study, the radiosonde and tethersonde data that was collected do not appear to capture evidence of a playa breeze return circulation, so in Section 5 model setup results will be examined for such evidence.

3.2. Model Experiments

3.2.1. Temperature Comparisons

Comparisons of model output with observation station data are performed for the same eight SAMS sites at the top of each hour—four located on the playa and four located off the playa—for each of the different setup experiments listed in Table 1. More specifically, model results at the nearest time-step closest to the top of the hour are compared to the 5-min averaged SAMS observation valid at the top of the hour. All model results shown from here, unless specifically noted otherwise, are for the 0.452 km inner nest. The aggregate surface temperature mean bias (MB), mean absolute error (MAE), and correlation-coefficient (R) values were calculated for the period of 0800 UTC Oct 14, 2012 through 0800 UTC Oct 15, 2012. A negative value indicates a cold model bias, whereas a positive value a warm model bias. The values for MB and MAE are summarized in Tables 2 and 3. The formulas for the mean bias, mean absolute error, and correlation coefficient are given as below where n = total number of hourly observations which here is 25. In addition, these computations are performed separately for each of the five model setups MS1–MS5 for each variable T 2 m AGL, U-component 10 m AGL, and v-component 10 m AGL:

$$\text{MB} = \frac{1}{n} \sum_{i=1}^{n} (M_i - O_i)$$

$$\text{MAE} = \frac{1}{n} \sum_{i=1}^{n} |M_i - O_i|$$

$$R = \left(\frac{\left(\sum_{i=1}^{n} (M_i - \overline{M})(O_i - \overline{O}) \right)}{\sqrt{\left(\sum_{i=1}^{n} (M_i - \overline{M})^2 \right) \left(\sum_{i=1}^{n} (O_i - \overline{O})^2 \right)}} \right).$$

Table 2. Aggregate 2 m AGL temperature mean bias values for each model setup.

SAMS Station	MS1	MS2	MS3	MS4	MS5
OFF PLAYA					
2	1.96	1.90	1.75	1.09	0.71
10	0.96	1.55	1.02	1.09	−0.05
22	1.45	2.12	1.67	1.31	0.12
31	−0.36	0.15	−0.26	0.15	−0.18
PLAYA					
9	0.48	0.86	0.36	0.65	−0.30
18	0.23	0.68	−0.02	0.30	−0.43
19	0.97	1.58	0.84	1.38	0.61
26	−0.13	0.67	−0.23	0.21	−0.65

Table 3. Aggregate 2 m AGL temperature mean absolute error values for each model setup.

SAMS Station	MS1	MS2	MS3	MS4	MS5
OFF PLAYA					
2	2.69	2.31	2.49	1.62	1.84
10	2.25	2.52	2.20	2.16	1.57
22	2.41	2.87	2.49	2.28	1.80
31	1.97	1.88	1.94	1.82	1.88
PLAYA					
9	1.31	2.02	1.69	1.81	1.47
18	0.93	1.59	1.34	1.37	1.41
19	2.11	2.83	2.36	2.81	2.55
26	1.09	1.97	1.52	1.80	1.42

Tables 2 and 3 show the performance of each model setup for the same playa and off-playa sites based upon the aggregate mean bias and aggregate mean absolute error for 2 m AGL surface temperature across all forecast times. It indicates that MS1 seems to have had a decent handle of the playa temperatures, especially in the afternoon, but that MS5 was clearly better for the off-playa sagebrush sites (especially for capturing the late-night cooling better on the night of 15 October). However, nearly all setups were too warm on the night and early morning of 14 October, although at site 26 (a playa site) some setups had a bit more success. One might at least consider that difficulties on the night of 14 October had something to do with errors in lower-tropospheric synoptic conditions introduced through the GFS and NAM. As indicated in Table 1, one of the factors that sets apart MS4 and MS5 is the fact that they used the formulation of [62] for computing the soil thermal conductivity parameter within Noah as recommended in [27] for silt loam and sandy loam soils (the prevalent soil type over the non-playa sagebrush region of DPG). Also, Ref. [27] concluded that its use in WRF resulted in a dramatic decrease in nighttime warm biases of 2 m AGL temperature over DPG. With respect to the playa-to-non-playa temperature gradients, it does not take an exceedingly large gradient to induce a playa breeze circulation component [74]. Thus, biases in predicting the surface heat fluxes which can then lead to slight model temperature biases (for example, perhaps introduced through biases in the Noah land surface model treatment of playa surfaces) can result in a weaker or stronger playa breeze simulation, and as to how much it contributes versus other components of the overall circulation (synoptic, valley, slope, and lake) [74].

All model setups were initialized from soil-moisture values interpolated from either the NAM or GFS grids, and no special high-resolution soil-moisture input fields were used, or adjustments performed. For each dominant land-use and soil-texture category determined for a grid cell, a reference to WRF tables (VEGPARM and SOILPARM) is used by the Noah land-surface option for defining static values of important parameters which are functions of the land use/vegetation or soil-texture class. It is possible that some of these parameter settings may be set for more generalized land-use and soil-texture characteristics, and not necessarily as well for the conditions that existed during this specific case. No attempt was made here to modify these tabular values. For example, in the case of MS1, it might be that the static table settings for the "barren or sparsely vegetated" land-use class could have fortuitously represented some of the playa conditions of that time better than the static settings for the actual "playa" land-use category used by the other setups. Precipitation that occurred just days before IOP6 could have also potentially broken up or disrupted some of the salt crust and salinity properties on the playa surface [68,69]. This action may have lowered the albedo (and increased the soil moisture) of the playa surface from those usually found during the month of October. In [74], suspected biases of the Noah land-surface model over playa surfaces are also discussed.

3.2.2. Wind Speed and Wind Direction Comparisons

Tables 4 and 5 show the surface aggregate mean bias and mean absolute error for the 10 m AGL u-wind component. Tables 6 and 7 show the same for the 10 m AGL v-wind component. The 10 m AGL wind speed and wind direction plots can also be referred to in Figure 8a–d, Figures 9a–d and 10 and Figure 11, respectively. Overall, there are no significant differences in the aggregate metrics of surface u-wind and v-wind components, and this is not surprising given that mean wind speeds throughout the event were quite low. A small positive 10 m AGL u-wind speed component bias does exist for all setups at all the sites, which could be a result of synoptic- or regional-scale forcing errors introduced from the GFS and NAM. Figures 8a–d and 9a–d show that all model setups reasonably captured small amplitude sub-diurnal oscillations in 10 m AGL wind speed through IOP6, although different errors in the phasing and frequency of these occurred across the different setups. During the second night of IOP6 into the morning of 15 October, there was a clear gradual increase of 10 m AGL wind speed observed at many of the sites (with alternating dips and spikes superimposed), likely a combination of playa, drainage, and synoptic influences. This was noted at both playa and non-playa sites, and across all setups.

Table 4. Aggregate 10 m AGL u-wind component mean bias values for each model setup.

SAMS Station	MS1	MS2	MS3	MS4	MS5
OFF PLAYA					
2	0.18	−0.23	−0.10	−0.06	−0.33
10	1.07	1.24	1.27	1.60	1.57
22	0.68	0.71	0.91	1.13	1.31
31	−0.46	−0.55	−0.34	−0.20	−0.05
PLAYA					
9	1.16	1.05	1.15	1.32	1.39
18	0.11	0.26	0.23	0.16	0.15
19	0.08	0.14	0.05	0.27	0.04
26	0.07	0.15	0.17	0.15	0.14

Table 5. Aggregate 10 m AGL u-wind component mean absolute error values for each model setup.

SAMS Station	MS1	MS2	MS3	MS4	MS5
OFF PLAYA					
2	1.10	1.44	1.26	1.81	1.46
10	1.32	1.34	1.42	1.63	1.66
22	0.93	0.99	1.05	1.18	1.41
31	0.99	1.02	0.94	1.26	1.08
PLAYA					
9	1.46	1.37	1.55	1.65	1.70
18	1.07	1.31	1.28	1.21	1.19
19	1.00	1.09	0.93	1.24	1.09
26	0.90	1.17	0.98	1.32	1.03

Table 6. Aggregate 10 m AGL v-wind component mean bias values for each model setup.

SAMS Station	MS1	MS2	MS3	MS4	MS5
OFF PLAYA					
2	0.41	0.57	0.32	0.75	0.11
10	−0.17	0.14	−0.27	−0.27	−0.34
22	−0.17	−0.13	−0.28	−0.12	−0.23
31	−0.24	0.18	−0.51	−0.09	−0.11
PLAYA					
9	0.17	0.15	0.01	−0.09	0.11
18	−0.87	−1.18	−1.07	−1.18	−1.33
19	−0.95	−1.55	−1.03	−2.01	−1.45
26	−0.48	−0.69	−1.10	−0.66	−1.00

Table 7. Aggregate 10 m AGL v-wind component mean absolute error values for each model setup.

SAMS Station	MS1	MS2	MS3	MS4	MS5
OFF PLAYA					
2	1.28	1.06	1.09	1.03	0.93
10	0.79	0.82	0.96	1.06	1.02
22	0.82	0.72	0.69	0.66	0.81
31	1.13	1.11	1.19	1.10	1.24
PLAYA					
9	1.05	0.74	0.94	0.80	1.06
18	1.15	1.31	1.28	1.39	1.58
19	1.12	1.69	1.22	2.09	1.68
26	1.63	1.52	1.68	1.34	1.70

Figures 10 and 11 show model versus observed 10 m AGL wind directions across the same SAMS sites. During the afternoon of 14 October, there were signs of a wind direction shift (especially in the model simulations) to a more west-to-northwest direction for a few hours at several sites located near the edge of the GSL Playa on the north end of the

Dugway Valley (sites 9, 10 and 22). Given the directions and location with respect to the GSL Playa edge, it is suggestive of a weak playa breeze circulation trying to get established. The model setups (especially MS4 and MS5) are supportive of this idea, even if they may be too aggressive. During the early morning hours of 15 October, all the model setups successfully captured on-playa 10 m AGL easterly flow and the transition to southeasterly downvalley flow along the Dugway Valley. Recall that during the first night (14 October) of the simulations, there was too much of a west—northwesterly flow component across Dugway Valley, including gap flow between Granite Peak and the Dugway Range. This, along with perhaps too much model drainage flow into the Dugway Valley off Granite Peak, resulted in a general retardation of east—southeasterly downvalley flow development in the model until around daybreak. Observations from the mini-SAMS network in the Dugway Valley support this idea until about 0800 UTC on 14 October, where after about 0900 UTC the transition to an extended period of weak downvalley flow becomes mostly established (while in the model this never really occurs until maybe 1300 UTC). On the 15 October, by 0800 UTC both the model and observations show a well-established downvalley flow through the Dugway Valley. Plots of the MS5 results showing 10 m AGL surface wind vectors and terrain elevation are shown in Figures 12 and 13 for the times of 0800 UTC Oct 14 and 0800 UTC Oct 15. Here MS5 was selected for plotting as it performed the best in terms of the 2 m AGL temperature metrics across the aggregate times and SAMS sites we compared. The SAMS observations (including special MATERHORN mini-SAMS observations) for 10 m AGL surface wind at both 0800 UTC Oct 14 and 0800 UTC Oct 15 are also shown in Figures 14 and 15 respectively. Plots of the MS5 results showing 10 m AGL surface wind vectors and terrain elevation are also shown in Figure 16 for 1300 UTC Oct 14. These figures add some clarity to the discussions above.
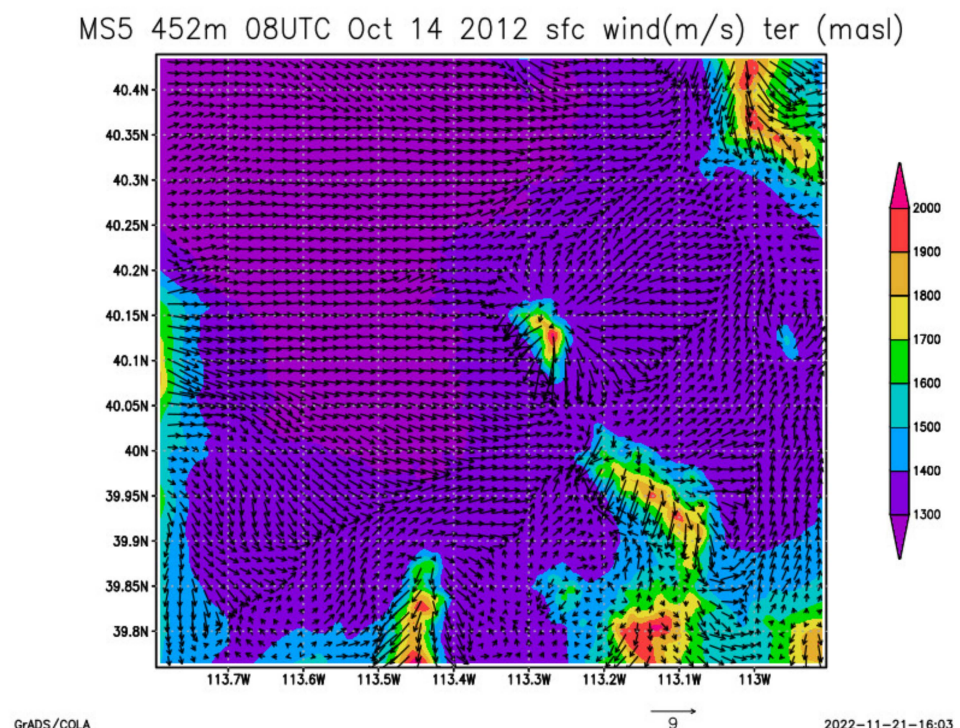

Figure 12. Model MS5 surface 10 m AGL wind vectors (m/s) for nest 4 (0.452 km), plotted over the model terrain (m ASL), valid at 0800 UTC 10-14-2012.
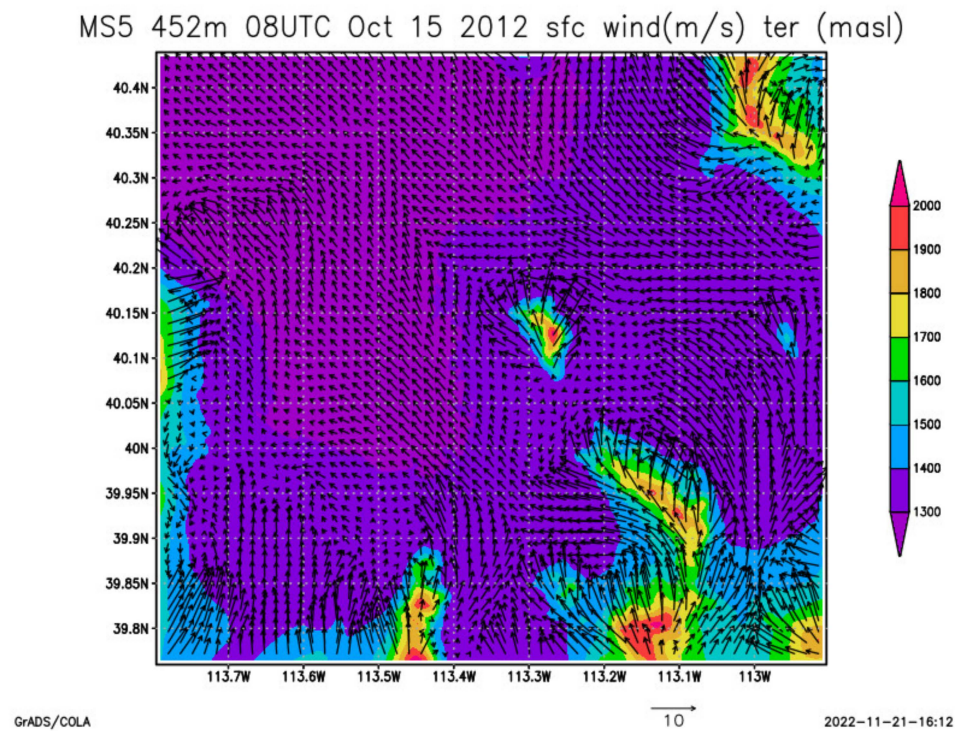
Figure 13. Model MS5 surface 10 m AGL wind vectors (m/s) for nest 4 (0.452 km), plotted over the model terrain (m ASL), valid at 0800 UTC 10-15-2012.
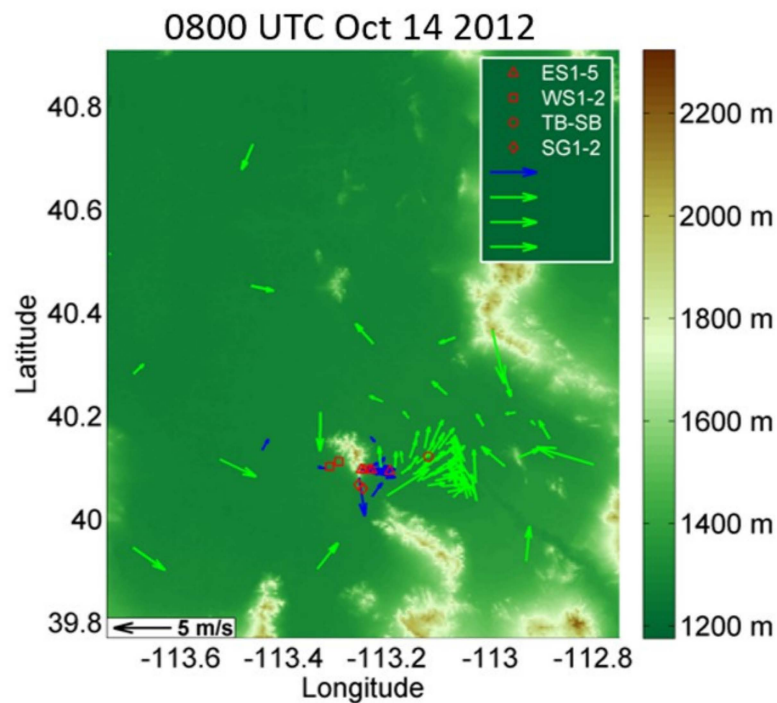

Figure 14. SAMS, mini-SAMS and other special MATERHORN 10 m AGL surface observations capturing flow over the GSL Playa, Granite Peak, and Dugway Valley at 0800 UTC 10-14-2012.
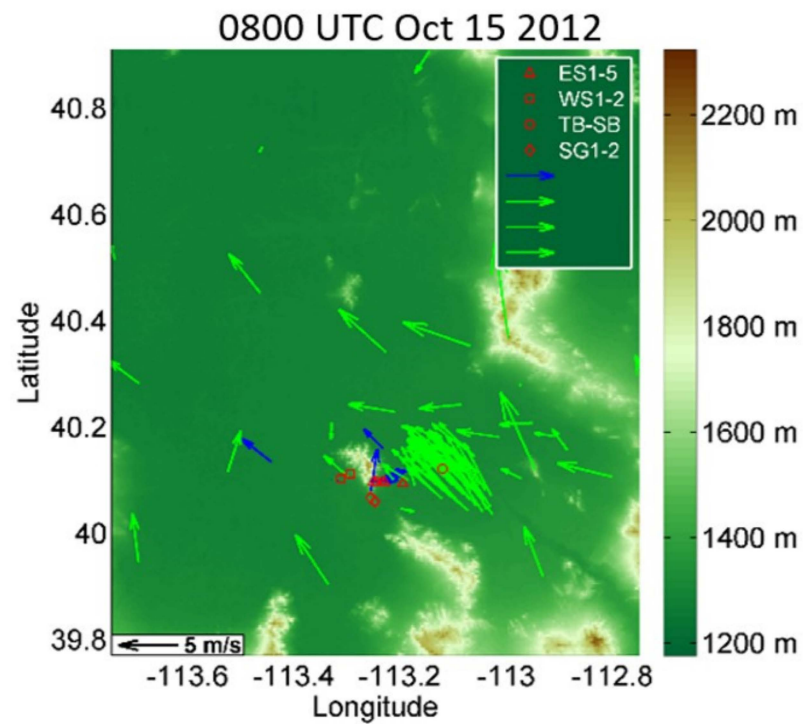
Figure 15. SAMS, mini-SAMS and other special MATERHORN 10 m AGL surface observations capturing flow over the GSL Playa, Granite Peak, and Dugway Valley at 0800 UTC 10-15-2012.
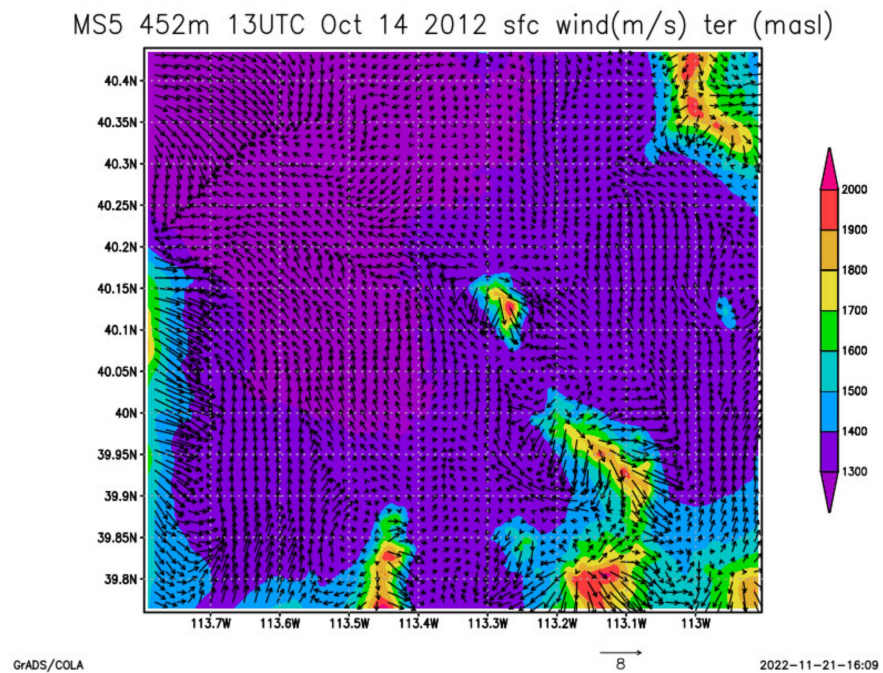

Figure 16. Model MS5 surface 10 m AGL wind vectors (m/s) for nest 4 (0.452 km), plotted over the model terrain (m ASL), valid at 1300 UTC 10-14-2012.

Finally, Tables 8–10 show the aggregate correlation-coefficient R values for 2 m AGL temperature, 10 m AGL u-wind component, and 10 m AGL v-wind component. As shown in Table 8, across the board for both playa and non-playa sites, the values of R indicate that there was strong positive correlation in 2 m AGL temperature between the model and observations when aggregated through IOP6. The off-playa sites two and thirty-one had

slightly reduced values of R (but still above 0.9 across all model setups), which may be an effect of their proximity to Granite Peak and the Dugway Range respectively.

Table 8. Aggregate 2 m AGL temperature correlation coefficient R values for each model setup.

SAMS Station	MS1	MS2	MS3	MS4	MS5
OFF PLAYA					
2	0.90	0.92	0.93	0.97	0.93
10	0.97	0.98	0.98	0.99	0.97
22	0.97	0.98	0.98	0.98	0.95
31	0.95	0.93	0.95	0.93	0.92
PLAYA					
9	0.98	0.97	0.97	0.97	0.96
18	0.99	0.97	0.98	0.98	0.97
19	0.99	0.97	0.98	0.98	0.98
26	0.97	0.96	0.96	0.95	0.97

Table 9. Aggregate 10 m AGL u-wind component correlation-coefficient R values for each model setup.

SAMS Station	MS1	MS2	MS3	MS4	MS5
OFF PLAYA					
2	0.52	0.43	0.50	0.25	0.42
10	0.72	0.81	0.77	0.81	0.80
22	0.84	0.80	0.83	0.84	0.80
31	0.82	0.78	0.87	0.76	0.84
PLAYA					
9	0.68	0.61	0.66	0.44	0.65
18	0.61	0.51	0.43	0.56	0.64
19	0.28	0.19	0.18	0.20	0.22
26	0.80	0.72	0.80	0.79	0.80

Table 10. Aggregate 10 m AGL v-wind component correlation-coefficient R values for each model setup.

SAMS Station	MS1	MS2	MS3	MS4	MS5
OFF PLAYA					
2	0.21	0.54	0.35	0.63	0.52
10	0.25	0.43	0.24	0.48	0.35
22	0.20	0.21	0.38	0.45	0.43
31	0.45	0.32	0.52	0.36	0.44
PLAYA					
9	0.03	0.30	0.19	0.30	0.20
18	0.67	0.72	0.72	0.59	0.50
19	0.83	0.71	0.86	0.70	0.80
26	0.15	-0.18	−0.21	−0.05	−0.13

For the 10 m AGL u-wind component, overall, the relationship was well captured between the model and observations as shown in Table 9. The lowest correlations are

found at off-playa site two and playa site nineteen, while the stronger correlations are at off-playa sites ten, twenty-two, and thirty-one. However, playa site 26 also shows a strong positive correlation for the u-component across the model setups. For the 10 m AGL v-wind component, the aggregate correlations tend to be weaker than for the u-wind component as shown in Table 10. The orientation of most of the terrain features being aligned more south-to-north may have some role in this. However, playa sites 18 and 19 differ from the other sites with stronger positive correlations for the v-wind component. Curiously, playa site 26 showed little to no (or even negative) correlation of v-wind through IOP6. One thought is that although sites 18, 19, and 26 are all on the playa, their orientation and distance to larger topography differ. In fact, it is quite possible that the low correlations in v-wind at site 26 had something to do with the model handling (across all model setups) of the anabatic and katabatic flows coming off the nearby Dutch Mountain. Site 26 is also closest to a lateral boundary of the 0.452 km nest than all other sites. Although the model setups showed little preference in terms of correlation coefficient for the u-wind component, for the v-wind component it appeared that both MS4 and MS5 performed better during IOP6 (with the exception being at site 26). Table 11 provides the coordinates of each SAMS site used in the comparison of the previous temperature and wind statistical metrics.

Table 11. SAMS site locations.

SAMS Station	Latitude	Longitude	Elevation
OFF PLAYA	Deg N	Deg W	m ASL
2	40.046	−113.208	1317.5
10	40.182	−113.022	1314.7
22	40.208	−112.960	1321.0
31	40.108	−113.307	1308.8
PLAYA			
9	40.243	−113.093	1309.8
18	40.116	−113.533	1294.9
19	39.904	−113.344	1306.1
26	40.282	−113.700	1292.0

3.2.3. Tethersonde Comparisons

Tethersondes released during 14 October of IOP6 assisted in evaluating how the setups reproduced three-dimensional aspects of the flow. Figures 17 and 18 illustrate the vertical temperature profiles obtained from the Playa (on-playa) site tethersonde releases at 1300 UTC and 2200 UTC, respectively, comparing them to the profiles produced across the various model setups. Figures 19 and 20 show the same except for the Sagebrush tethersonde site near Granite Peak (off-playa).

At the Playa site, the 1300 UTC morning inversion is apparent and captured using all model setups. However, model setups MS1, MS3, and MS5 underpredict the strength of the inversion, while MS2 and MS4 handle it better. Both MS2 and MS4 do a good job capturing the temperature at the top of the shallow inversion which was observed as 12.5 deg C at 860 hPa (MS2 predicts 12.75 deg C, and MS4 predicts 12.5 deg C). However, MS2 predicts the inversion top at about 868 hPa and MS4 at about 875 hPa. Additionally, MS2 and MS4 both showed too small a magnitude of radiative cooling from the inversion top down to 2 m AGL. In fact, all the setups showed this deficiency at this time and location. It is interesting to note that although MS5 did produce a significantly cooler inversion top at a level in between those of both MS2 and MS4, it also produced a comparable degree of cooling to the surface so ends up looking better when compared to observed temperatures in the lowest 5 hPa above the surface or so. It should be noted here that in the plots each setup's diagnostic 2 m AGL temperature value is not plotted, so modeled

temperatures at the surface would resemble the tethersonde curve a little more closely with those incorporated (the lowest model half-level plotted is at about 12 m AGL). The key difference in MS2 and MS4 were that they were the only members to use GFS rather than NAM for boundary conditions, so external model forcing conditions do seem to matter in IOP6. Another thing to mention is that both MS4 and MS5 used the thermal soil conductivity which is expected to most impact nocturnal cooling over silt-loam and sandy-loam soil types. At 2200 UTC, the model temperature profiles were all too cool by about a degree or two through the lowest 40 hPa of the boundary layer compared to those from the Playa tethersonde, although MS1 was the warmest member and the closest to observations. However, all members showed afternoon unstable profile structures that closely resembled the tethersonde, although not quite capturing the full magnitude of surface warming (MS1 again being the closest).

Figure 17. Model upper-air temperature profile (°C) shown by pressure level (hPa) for different model experiments vs. tethersonde at 1300 UTC 10-14-2012 at the Playa site.

Figure 18. Model upper-air temperature profile (°C) shown by pressure level (hPa) for different model experiments vs. tethersonde at 2200 UTC 10-14-2012 at the Playa site.
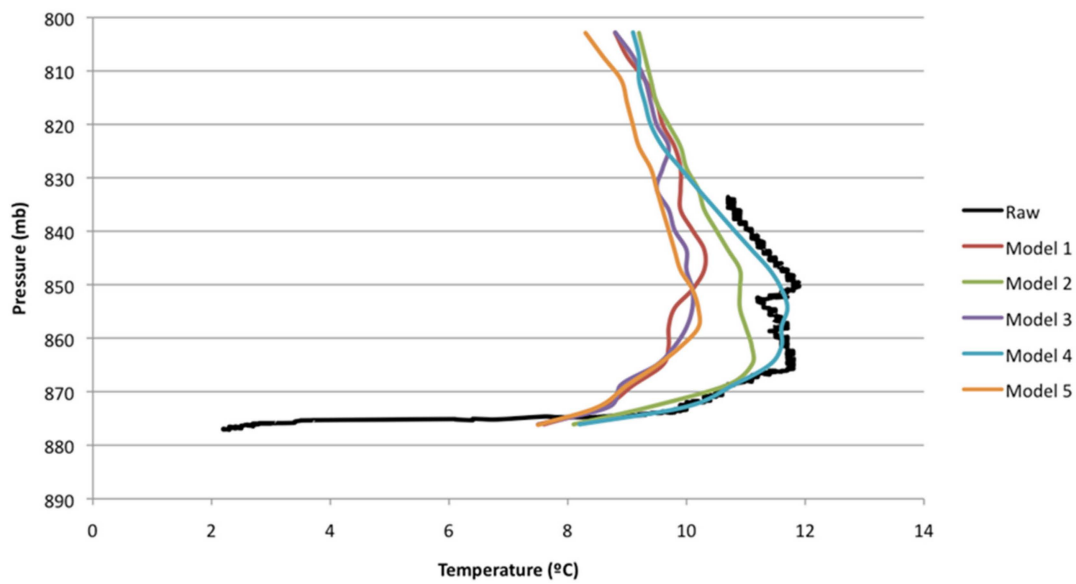
Figure 19. Model upper-air temperature profile (°C) shown by pressure level (hPa) for different model experiments vs. tethersonde at 1300 UTC 10-14-2012 at the Sagebrush (off-playa) site.
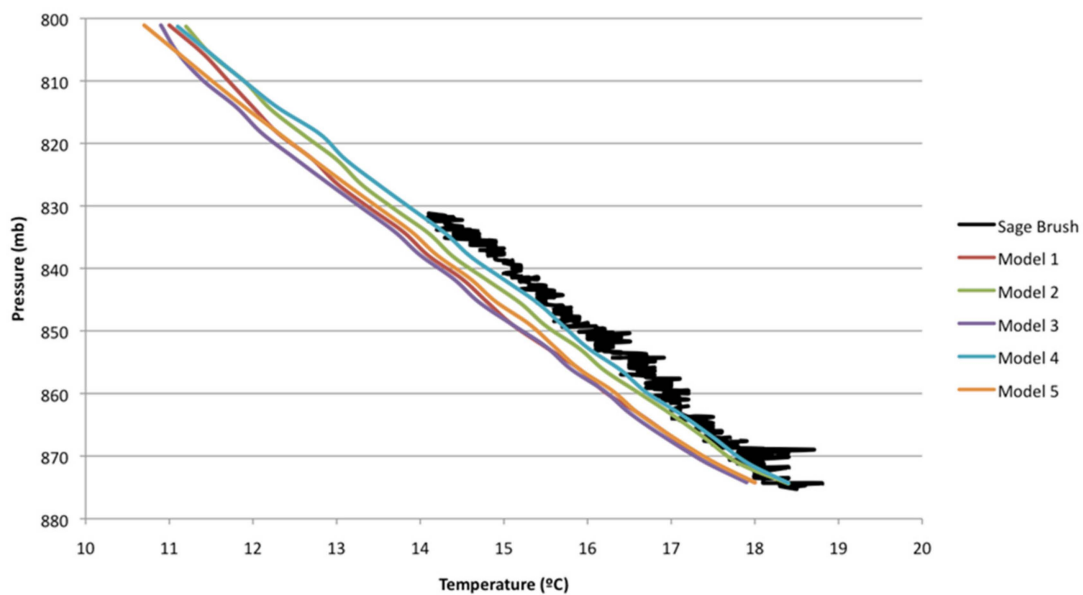

Figure 20. Model upper-air temperature profile (°C) shown by pressure level (hPa) for different model experiments vs. tethersonde at 2200 UTC 10-14-2012 at the Sagebrush (off-playa) site.

For the Sagebrush (off-playa) tethersonde site, the model setups MS2 and MS4 (the two that used GFS forcing) are again superior as they were at the Playa tethersonde site during the morning at 1300 UTC. The GFS-forced setups provided a more realistic and warmer overall boundary layer structure and morning inversion top as compared to the NAM-forced setups. None of the five setups captured the total magnitude of the stable temperature inversion right near the ground particularly well. At 2200 UTC, most of the setups yielded unstable profiles but were a bit cooler than observed during the afternoon throughout the depth of the boundary layer. However, the MS4 setup had a profile quite close to the tethersonde observations with the MS2 setup close as well (both again used GFS forcing conditions).

Examining the wind direction profiles in the morning boundary layer, the 1300 UTC model profiles are compared to the concurrent tethersonde released at the Playa site

(Figure 21). Within the lowest few hundred meters or so (lowest ~30 hPa) there is reasonable agreement across all the setups. However, the shift in the simulations of wind direction at the Playa site to northwesterly flow aloft starts considerably lower in the atmosphere than what is indicated by the tethersonde, while the directions were also more northerly than easterly between about 875 hPa and 860 hPa. A similar type of pattern in wind direction shift seems to occur at the Sagebrush (off-playa) site at 1300 UTC (Figure 22). A difference at the Sagebrush site versus the Playa site is that the wind direction observations are more northerly versus northwesterly above 860 hPa. The Playa 14 October morning radiosonde (not shown) shows the switch to a northwesterly flow aloft not occurring until about 780 hPa. These differences seem to offer hints as to why the model 10 m AGL surface winds across Dugway Valley may have struggled to switch to a more established downvalley flow direction on the night and morning of 14 October. The 2200 UTC model winds were not compared to either tethersonde site, due to the messy light and variable boundary layer wind conditions of both the simulations and observations under the convectively unstable afternoon conditions.
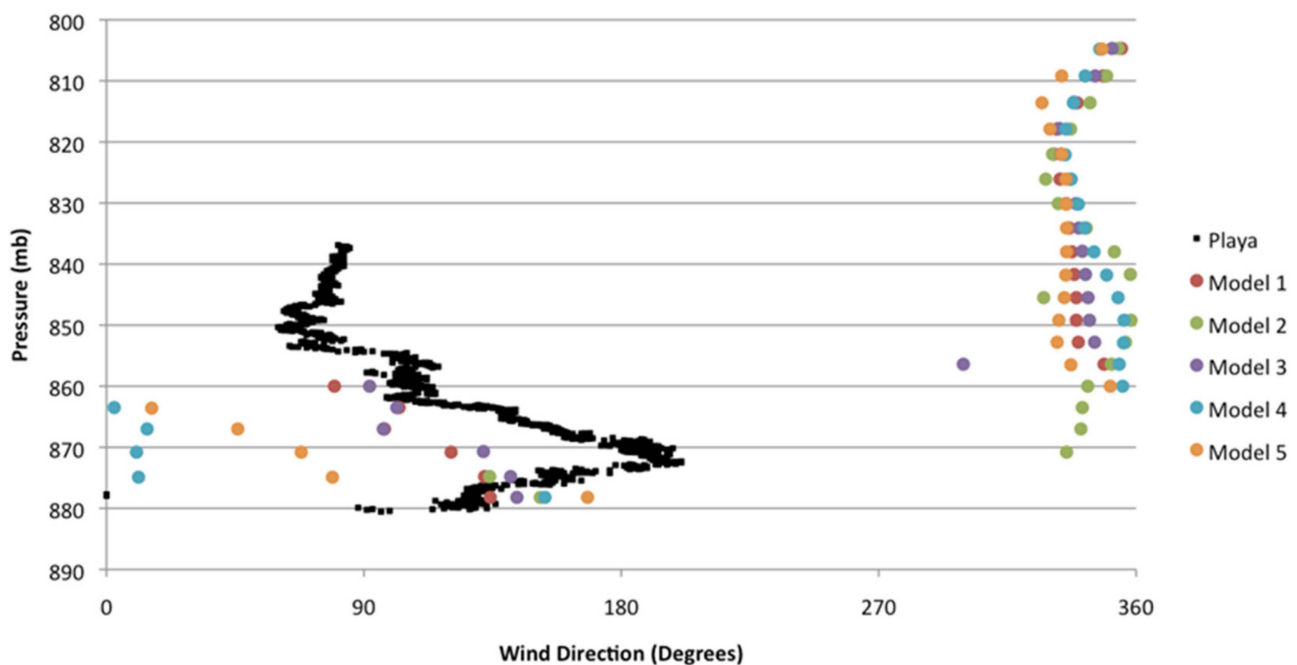

Figure 21. Model upper-air wind direction profile (°) shown by pressure level (hPa) for different model experiments vs. tethersonde at 1300 UTC 10-14-2012 at the Playa site.

In general, additional radiosondes released (not shown) in the study region showed that winds above 700 hPa tended to have a westerly component throughout IOP6 over both the Playa and Sagebrush regions, although more north—northwesterly on the night of 14 October and west—northwesterly on the night of 15 October. The large-scale geostrophic flow at 700 hPa tended to remain close to 5 m/s (although increasing to as much as 20 m/s above 400 hPa) through IOP6 and remained mostly less than 5 m/s below 700 hPa.
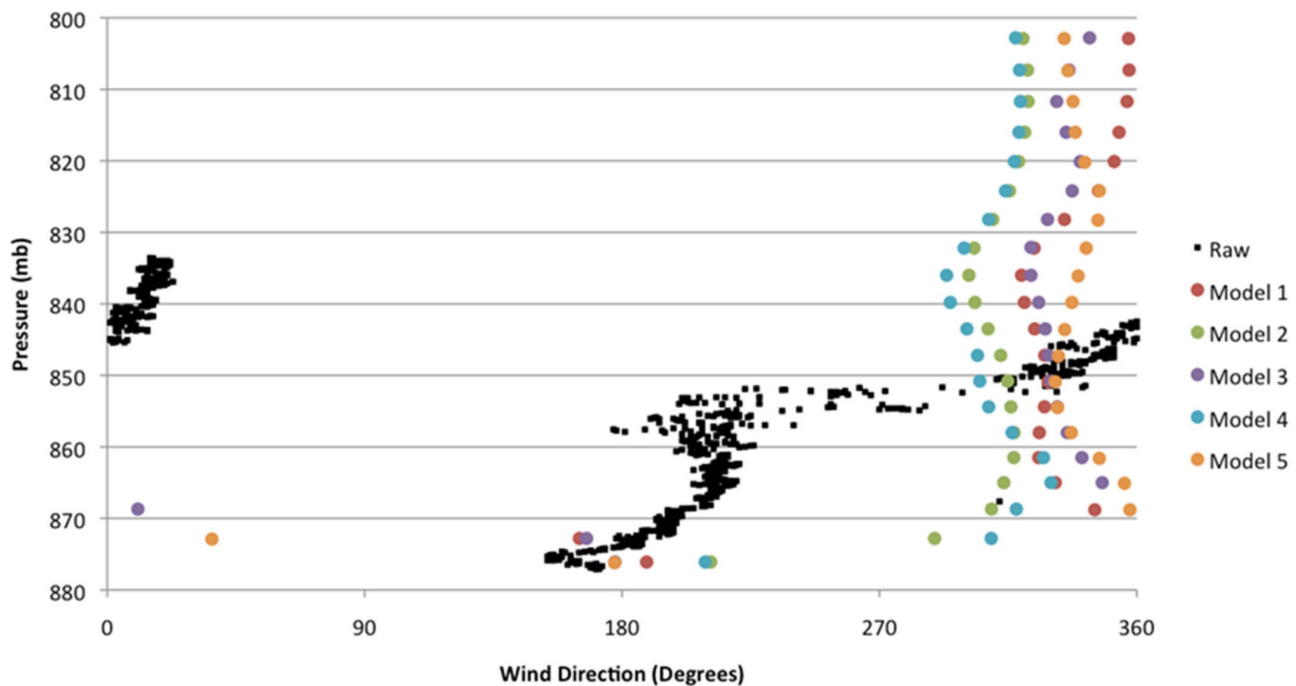
Figure 22. Model upper-air wind direction profile (°) shown by pressure level (hPa) for different model experiments vs. tethersonde at 1300 UTC 10-14-2012 at the Sagebrush (off-playa) site.

4. Discussion of Modeled Diurnal Thermodynamically Forced Flows

Local mesoscale circulations, due to the complex terrain and land use, typically become more evident in the DPG region as model resolutions approach 1 km grid spacing. Even at 4.067 km grid spacing, some of these circulations start to become resolved by the simulations, such as the lake breeze around the Great Salt Lake (not shown). Overall, although the large-scale flow is weak there was apparently enough modeled flow at around 850 hPA that the diurnal flow regime in the simulations introduced a bit of a westerly flow bias on 14 October around the eastern GSL Playa and Granite Peak/Dugway Valley areas. This also appears to have delayed or diminished the typical Dugway Valley southeasterly downvalley flow evolution on the night of 14 October. The evolution to nocturnal downvalley southeasterly flow across the Dugway Valley occurs in the model setups much more in line with expectation (and observations) on the night and morning of 15 October.

4.1. Playa Breeze

Although examination of the 0.452 km nest surface-wind fields both off and on the GSL Playa showed some evidence in 2D of a playa breeze circulation during IOP6 (on the late afternoon of 14 October) as noted previously, we explored the model output data further to look for additional evidence of a circulation in 3D.

Only the vertical cross sections for a single model setup are examined here for brevity, and setup MS5 is again selected because it performed well for both playa and off playa locations in the handling of the surface temperature field (discussed previously). A return flow of a direct thermal circulation (such as a playa breeze) can be identified via winds in the upper branch of the circulation flowing in an opposite direction to those in the lower branch near the surface (in addition to opposing ends of the circulation showing contrasting upward and downward vertical motion). Figure 23 shows the 2200 UTC model 10 m AGL surface wind vector field over the model terrain. In addition, a red line shows where a 2200 UTC model meridional vertical cross section (along −113.18 deg W) is shown in Figures 24 and 25. In Figure 24, the positive v-wind component provides some evidence of a return circulation aloft near half-sigma level 20 (~750 m AGL) indicating a southerly

flow direction, while the near-surface flow shows an opposing negative v-wind (a northerly direction that is off-playa). The point along the cross section at the surface where the breeze appears to initiate in the model setup MS5 (suggested by the surface divergence in the flow) is close to 40.25 deg N at 2200 UTC. Figure 25 extends along the same cross section at 2200 UTC, except in this case it shows black contours of w and white contours of relative humidity drawn over shaded isotherms of the v-wind component. At about 40.17 N, there is a zone near the surface convergence boundary where there is an enhanced upward vertical motion to about half-sigma level 12 or around 400 m AGL (which culminates in an increased relative humidity at that level), and then generally weak downward vertical motion to the north back out to the playa. Therefore, between about latitudes 40.15 N and 40.26 N along the −113.18 deg W cross section, there is some evidence based upon the model that at least a weak playa breeze circulation was present. The winds are quite light and variable at both the Sagebrush radiosonde and tethersonde (−113.13 deg W; 40.12 deg N) sites taken at 2217 UTC (not shown) and do not offer convincing evidence of such a playa breeze circulation.
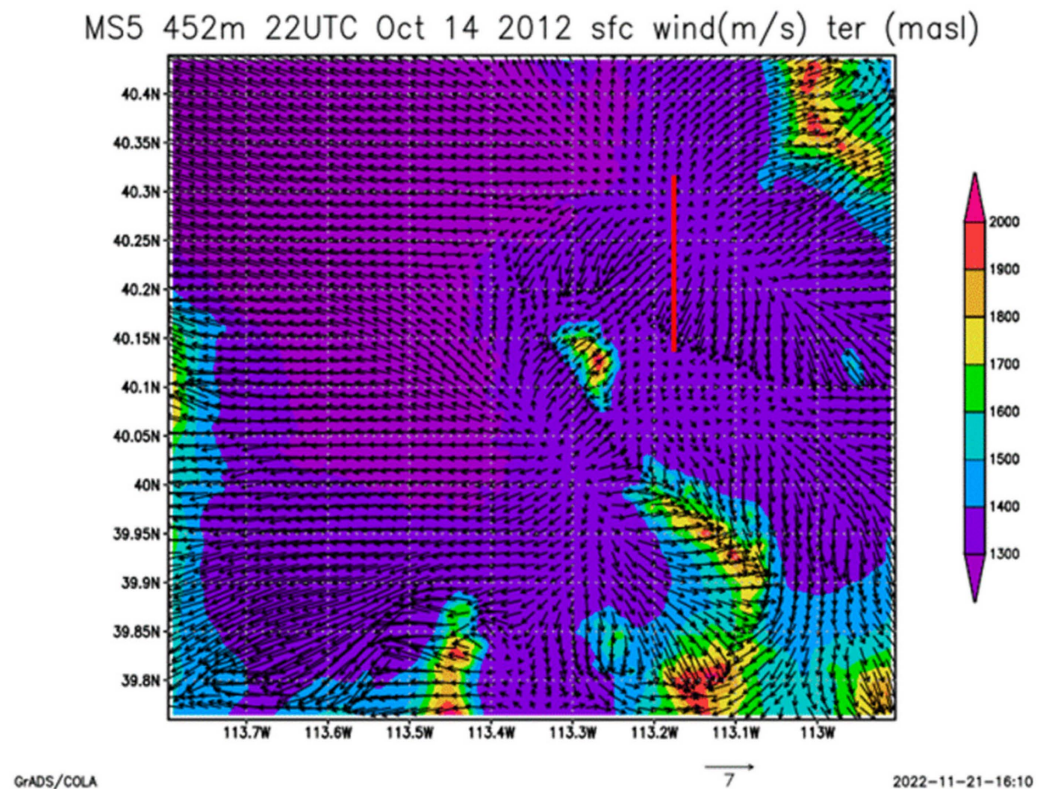

Figure 23. Model MS5 surface wind vectors (m/s) for nest 4 (0.452 km), plotted over the model terrain (m ASL), valid at 2200 UTC 10-14-2012. Red line shows meridional cross section used in subsequent plots.
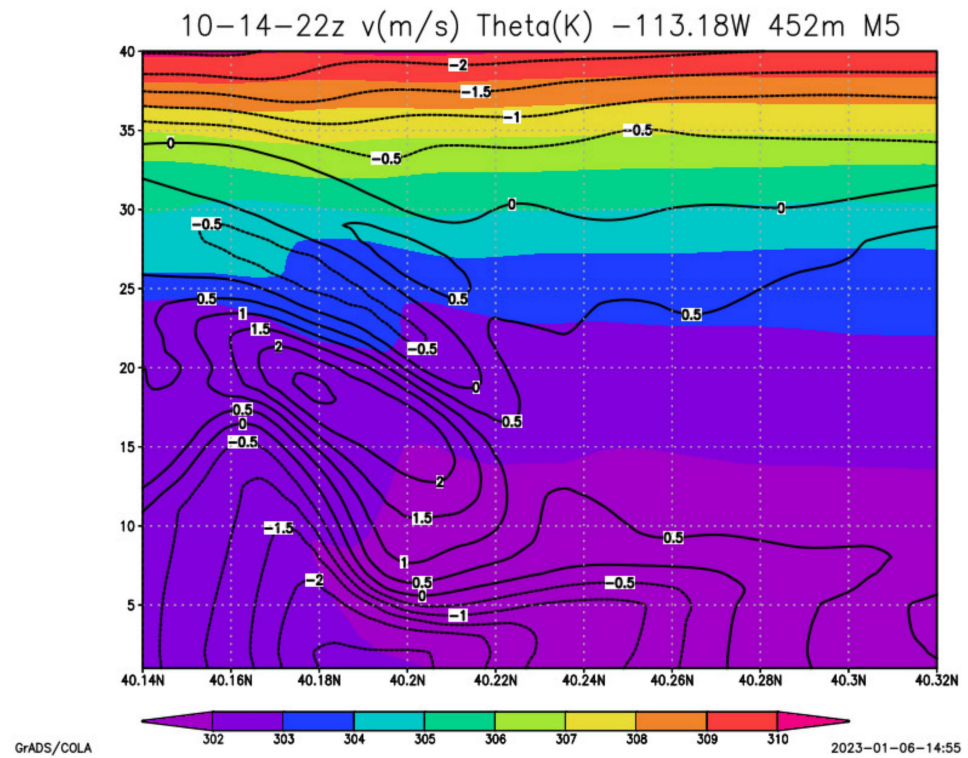
Figure 24. Model MS5 shaded "theta" (°K) and black contours of v-wind component (m/s) for the cross section along −113.18 W shown in the previous Figure 23. Vertical units are half-sigma levels, with level 20 at 749 m AGL, level 30 at 1330 m AGL, and level 40 at 2246 m AGL.
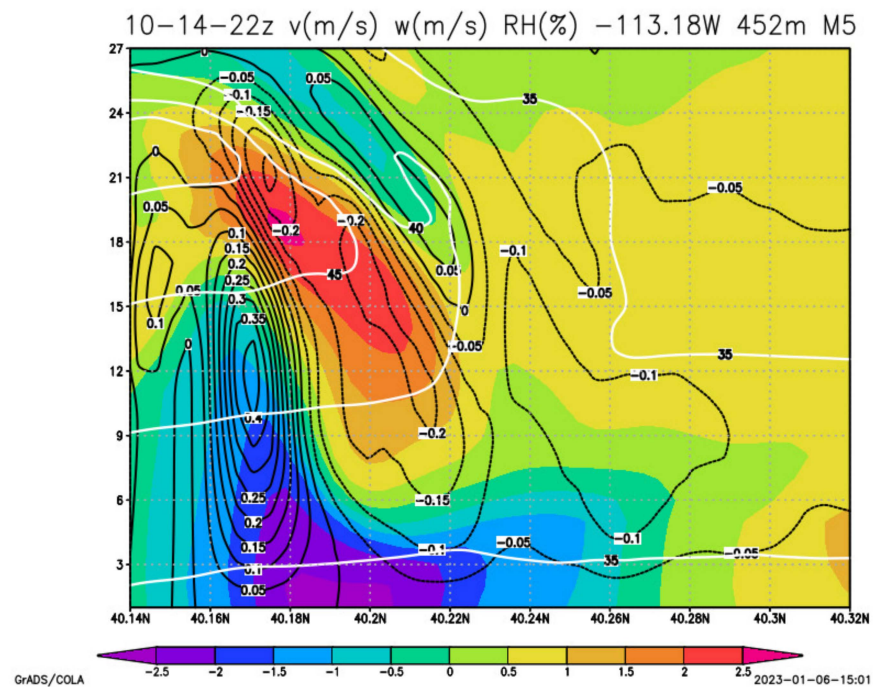

Figure 25. Model MS5 shaded v-wind component (m/s), RH (%) in white contours, and vertical motion w (m/s) in black contours for the cross section along −113.18 W shown in the previous Figure 24. Vertical units are half-sigma levels, with level 15 at 528 m AGL, level 20 at 749 m AGL, level 25 at 1010 m AGL, and level 27 at 1129 m AGL.

4.2. *Katabatic/Anabatic and Upvalley/Downvalley Flows*

The MS5 setup's reproduction of diurnal katabatic/anabatic and downvalley/upvalley flow systems observed around DPG during 14 October is now examined. Revisiting Figure 22, the 14 October 1300 UTC tethersonde wind direction, wind speed, and temperature measurements for the Sagebrush site are shown. The wind-direction panel indicates that a pronounced downvalley south—southeasterly flow established itself during the early morning hours, at least up through the first 200 m AGL. Figures 11, 14, and 15 also capture in the observations the nocturnal south-to-southeasterly downvalley flow through the Dugway Valley (especially the night of 15 October).

The MS5 surface 10 m AGL wind field for 1300 UTC 14 Oct shown in Figure 16 does capture some downvalley flow in the vicinity of the Sagebrush tethersonde site within the Dugway Valley. The MS5 also picks up a clear downvalley flow on the night of 15 October in Figure 13. Where the Dugway Valley and the GSL Playa are in proximity, there may be a coexistence of on-playa, downvalley, katabatic, and even gap flows. During the preceding hours between about 0800 UTC to 1200 UTC, the model generally struggled in firmly establishing the downvalley flow component on 14 October, with too much of either a westerly or northerly flow component often present (not shown). On the following night of 15 October, the downvalley flow was more developed throughout the night and morning in both the model and observations. In another study, the use of a modified non-local PBL layer turbulence scheme during stably stratified conditions did generate a somewhat improved downvalley flow over Dugway Valley throughout the night of 14 October [70]. During the afternoon at 2200 UTC 14 Oct, only a weak and disorganized northwesterly upvalley flow seems to have been established, and more across the southern end of the Dugway Valley. The MS5 captures this in Figure 23, as did some of the mini-SAMS observations through the afternoon (not shown). Like the downvalley situation, in the proximity of the Dugway Valley and GSL Playa there appears to exist a combination of different mesoscale flows probably existing at the same time (off-playa, upvalley, and anabatic).

The anabatic and katabatic flows are easy to pick out from the SAMS and mini-SAMS observations, such as around Granite Peak. In addition, the model setups (such as in Figures 16 and 23 for MS5) clearly develop flows driven by thermodynamic differences from the sloping complex topography. In fact, on the night of 14 October there was probably too much katabatic flow off the east-facing slopes of Granite Peak flowing into the Dugway Valley (possibly from the general westerly and northwesterly bias in flow across the region, likely from the synoptic forcing models). In addition, the low (and even negative) v-wind correlation values at playa site 26 across all the model setups could indicate issues with the model handling of the anabatic and katabatic flow (such as timing and extent) near to this specific location (which is near to Dutch Mountain).

5. Conclusions

This research utilized nested sub-kilometer grid spacing simulations of the WRF to study various diurnal mesoscale breeze systems common around the DPG, in the North American Great Basin Desert. Five model setups (MS1-MS5) were performed for this study, each initialized with a different set of parameterization schemes and large-scale input conditions as summarized in Table 1. Simulation output from each model setup was compared to SAMS measurements, in addition to special MATERHORN radiosonde and tethersonde data.

A review of SAMS wind speed and wind direction data both on and off the GSL Playa suggested that a weak playa breeze occurred along the northern end of the Dugway Valley during 14 October, with a sharp (and short duration) shift in winds to off-playa direction evident in the late-afternoon hours. The overall conclusion examining the simulations (particularly focused upon MS5) and observations is that the afternoon playa breeze was poorly established, despite the simulations showing a bit stronger and sustained circulation over a few hours. Throughout the majority of IOP6, observed and modeled 10 m AGL surface winds near much of the eastern edge of the playa maintained a more on-playa

direction with an easterly component (except in the simulations on the night of 14 October). In addition to the simulations producing a stronger and somewhat longer lasting afternoon off-playa breeze than was observed on 14 October, there were also hints in the MS5 setup's meridional vertical cross sections of a weak return flow between levels of about 400–700 m AGL. There was no such model evidence of this kind of return flow at night during the on-playa flow phase, which would have been much lower due to static stability considerations. The special MATERHORN Sagebrush and Playa radiosondes and tethersondes failed to capture any distinct upper-branch return circulation of a playa breeze at any launch time throughout the IOP6.

After examining the 10 m AGL surface winds from the 0.452 km nest of each setup, it seemed likely that many aspects of previously discussed DPG flow forcing [15,27,51,65] seemed to be active during the IOP6 studied here, and that clearly a tertiary set of local mesoscale flows were often superimposing upon one another making isolation of one from the other often difficult (on/off playa, anabatic/katabatic, and upvalley/downvalley). In addition, at night the gap flow between Granite Peak and the Dugway Mountains also added more complexity, as did the interplay between drainage flows off the east slopes of Granite Peak and the downvalley flow over the Dugway Valley. Although not shown, after examining the output of the courser 4.067 km grid spacing nest (which covers a much larger areal domain), it seems plausible that a fourth mesoscale flow system (lake breeze system) can also contribute locally under different synoptic situations [15,65]. For example, under a northerly synoptic flow and Dugway Valley upvalley flow during the afternoon. The temporal evolution of 10 m AGL surface wind speed patterns throughout IOP6 appeared reasonably captured using the model versus SAMS observations. However, they were often out of phase in terms of the wind speed maxima/minima amplitudes within the sub-diurnal frequency oscillations observed through the period. Some of this phasing error would likely be improved by increasing the averaging frequency of the model output and the raw SAMS observations [71]. In addition, the WRF name list feature "tslist" allows point files of WRF surface and sigma-level forecast variable output to be made at every model timestep (for any nest). The overall low mean 10 m AGL surface wind speeds throughout the IOP6 led to wind metrics that did not show large errors, and that also did not show a significant difference between the model setup members. However, biases were a bit towards a slightly-too-much zonal and slightly-too-little meridional flow component at the surface throughout IOP6.

The model setups for 2 m AGL surface temperatures tended to be several degrees centigrade warmer than observed in the early morning hours and slightly cooler than observed during the mid—late afternoon. However, the use of the different soil thermal conductivity parameterization appears to have improved the late night/early morning warm bias across SAMS sites located in the Dugway Valley and over the Sagebrush location near Granite Peak. Other factors such as the choice of diffusion level option, radiation scheme, and PBL turbulence scheme seem to have had lesser effects. MS1, which was the only setup initialized with the lower resolution land-use dataset and with the absence of the additional playa, white sand and lava land-use and soil-texture categories produced slightly better 2 m AGL surface temperature simulations over the playa. Curiously, the MS3 member which was initialized with all the same parameterization schemes as MS1 except for the land-use and soil datasets produced slightly worse 2 m AGL surface temperature metrics over the GSL Playa than MS1. This may be in some way due to rainfall that occurred a few days before the start of IOP6, which could have broken up the salt crust of the playa and thereby may have lowered its albedo for many days. This may have resulted in certain tabular property values out of VEGPARM.TBL and SOILPARM.TBL (used by the Noah land-surface model in WRF) that were closer to those observed at the time than those given for actual playa land-use and soil categories in the same static tables (used by the other setups outside of MS1).

In terms of the boundary-layer temperature profiles above the surface, the simulation results seem to clearly indicate that the two members that used forcing from the GFS (MS2

and MS4) handled the depth and temperature at the top of the morning inversion of 14 October better. The NAM-forced members (MS1, MS3 and MS5) were several degrees too cool at the inversion top over both the Playa and non-playa/Sagebrush locations, although they may have shown a little more complexity in the profiles. All setups struggled with the degree of near-surface radiational cooling in the inversion profile within about 5 hPa of the surface. This is where the use of the different soil thermal conductivity formulation appears to have helped both MS4 and MS5 over some of the non-playa locations, although it is likely not the only factor.

Future extensions to this work are planned to consider how to better address the treatment of surface and boundary layer turbulence in the mesoscale turbulence gray area between about 200 m and 2 km grid spacing [78–81]. In this study, turbulence was handled through the use of a traditional mesoscale PBL local-parameterization scheme (either MYJ or QNSE). However, although the afternoon convective boundary layer depth was not particularly deep for IOP6, the gray area effects can start manifesting at an equivalent grid spacing distance close to that of the boundary layer depth. At 400 m grid spacing, it can be expected that gray area effects could be introduced during the convectively unstable period of IOP6 (which still had depths of over 2200 m ASL, or about 800–900 m AGL). Similarly, during the period of nocturnal stable-stratification conditions, adding an additional nest closer to around 50 m grid spacing might help in the vicinity of the Dugway Valley and Granite Peak. To do this effectively, we may wish to consider skipping the span of gray area range in the WRF by nesting directly from a mesoscale resolution using boundary-layer parameterization (such as 2 km grid spacing) to one using the LES option in WRF (such as 200 m grid spacing). Any additional finer nests would also be treated as LES. Such an approach is discussed in [82] and might avoid difficulties with model-dependent boundary-layer roll structures as noted in [83].

If successful with the nesting from mesoscale-to-LES, we then will look at focusing more upon specific boundary-layer processes critical to fine-scale flow behaviors such as the interactions between competing mesoscale-gamma flow systems and sub-mesoscale meandering behavior under stable stratification [84–87], soil moisture initialization [74], testing new approaches to address the limitations of classic Monin—Obukhov similarity profiles for the atmospheric surface layer [88], and experimenting with both mosaic and dynamic land-use treatment [89,90]. For stable stratification conditions, use of model LES nesting along with finer vertical layering (perhaps use of vertical nesting) near the surface are also likely to become important [84]. This will require use of the latest WRF V4 generation software, to leverage its later options for the use of a hybrid vertical coordinate [91] and vertical nesting [92] (along with many other software changes and bug fixes). Finally, even under apparent weak large-scale synoptic forcing, it is apparent that errors from the large scaler models supplying external lateral-boundary conditions can still have an influence on the evolution of local flows. Therefore, thought should be given to the synoptic conditions driving the mesoscale and microscale even in such scenarios where it might seem that such forcings should have only minor significance and receive only passing attention.

References

1. Skamarock, W.C.; Klemp, J.B. A time-split nonhydrostatic atmospheric model for weather research and forecasting applications. *J. Comput. Phys.* **2008**, *227*, 3465–3485. [CrossRef]
2. Crawford, T.; Stensrud, D.; Mora, F.; Merchant, J.; Wetzel, P. Value of incorporating satellite—Derived land cover data in MM5/PLACE for simulating surface temperatures. *J. Hydrometeorol.* **2001**, *2*, 453–468. [CrossRef]
3. Yu, M.; Carmichael, G.R.; Cheng, Y.F. Sensitivity of predicted pollutant levels to urbanization in China. *Atmos. Environ.* **2012**, *60*, 544–554.
4. Hawkes, H.B. Mountain and Valley Winds with Special Reference to the Diurnal Mountain Winds of the Great Salt Lake Region. Ph.D. Thesis, Ohio State University, Columbus, OH, USA, 1947; p. 312.
5. Hocut, C.; Liberzon, D.; Fernando, H. Separation of upslope flow over a uniform slope. *J. Fluid Mech.* **2015**, *775*, 266–287. [CrossRef]
6. Poulos, G.S. The Interaction of Katabatic Winds and Mountain Waves. Ph.D. Thesis, Colorado State University, Fort Collins, CO, USA, 1996; p. 297.
7. Fedorovich, E.; Shapiro, A. Structure of numerically simulated katabatic and anabatic flows along steep slopes. *Acta Geophys.* **2009**, *57*, 981–1010. [CrossRef]
8. Drake, S.; Higgins, C.; Pardyjak, E. Distinguishing Time Scales of Katabatic Flow in Complex Terrain. *Atmosphere* **2021**, *12*, 1651. [CrossRef]
9. Defant, F. Local Winds. In *Compendium of Meteorology*; Malone, T.F., Ed.; American Meteorological Society: Boston, MA, USA, 1951.
10. Barr, S.; Orgill, M. Influence of External Meteorology on Nocturnal Valley Drainage Winds. *J. Appl. Meteorol.* **1989**, *28*, 497–517. [CrossRef]
11. Mahrt, L.; Larsen, S. Relation of slope winds to the ambient flow over gentle terrain. *Bound. Layer Meteorol.* **1990**, *53*, 93–102. [CrossRef]
12. Mursch-Radlgruber, E. Observations of flow structure in a small forested valley system. *Theor. Appl. Climatol.* **1995**, *52*, 3–17. [CrossRef]
13. Poulos, G.; Bossert, J.T.; Pielke, R.S. The Interaction of Katabatic Flow and Mountain Waves. Part I: Observations and Idealized Simulations. *J. Atmos. Sci.* **2000**, *57*, 1919–1936. [CrossRef]
14. Serafin, S.; De Wekker, S.; Knievel, J. A Mesoscale Model—Based Climatography of Nocturnal Boundary—Layer Characteristics over the Complex Terrain of North—Western Utah. *Bound. Layer Meteorol.* **2015**, *159*, 495–519. [CrossRef]
15. Rife, D.L.; Warner, T.; Chen, F.; Astling, E.G. Mechanisms for Diurnal Boundary Layer Circulations in the Great Basin Desert. *Mon. Weather Rev.* **2002**, *130*, 921–938. [CrossRef]
16. Whiteman, C.D. *Mountain Meteorology: Fundamentals and Applications*; Oxford University Press: Oxford, UK, 2000; p. 355.
17. Thyer, N. A theoretical explanation of mountain and valley winds by a numerical method. *Arch. Für Meteorol. Geophys. Und Bioklimatol. Ser. A* **1966**, *15*, 318–348. [CrossRef]
18. Demko, J.C.; Geerts, B. A Numerical Study of the Evolving Convective Boundary Layer and Orographic Circulation around the Santa Catalina Mountains in Arizona Part I: Circulation without Deep Convection. *Mon. Weather Rev.* **2010**, *138*, 1902–1922.
19. Gleeson, T.A. Effects of Various Factors on Valley Winds. *J. Atmos. Sci.* **1953**, *10*, 262–269. [CrossRef]
20. Rampanelli, G.; Zardi, D.; Rotunno, R. Mechanisms of Up-Valley Winds. *J. Atmos. Sci.* **2004**, *61*, 3097–3111. [CrossRef]
21. Chiao, S.; Dumais, R. A down-valley low-level jet event during T-REX 2006. *Meteorol. Atmos. Phys.* **2013**, *122*, 75–90. [CrossRef]
22. De Wekker, S.; Liu, Y.; Knievel, J.; Pal, S.; Emmitt, G.D. Observations and Simulations of the Wind Structure in the Boundary Layer around an Isolated Mountain during the Materhorn Field Experiment. In Proceedings of the American Geophysical Union Meeting, San Francisco, CA, USA, 9–13 December 2013.

23. Bluestein, H. *Synoptic—Dynamic Meteorology in Midlatitudes Volume 1 Principles of Kinematics and Dynamics*; Oxford University Press: New York, NY, USA, 1992.

24. Tapper, N.J. Evidence for a mesoscale thermal circulation over dry salt lakes. *Palaeogeogr. Paleoclimatol. Paleoecol.* **1991**, *84*, 259–269. [CrossRef]

25. Physick, W.L.; Tapper, N.J. A Numerical Study of Circulations Induced by a Dry Salt Lake. *Mon. Weather Rev.* **1990**, *118*, 1029–1042. [CrossRef]

26. Pleim, J.; Ran, L.; Gilliam, R. New High-Resolution Land—Use Data in WRF. In Proceedings of the 10th WRF User's Workshop, Boulder, CO, USA, 23–26 June 2009.

27. Massey, J.; Steenburgh, J.; Hoch, S.; Knievel, J. Sensitivity of near—surface temperature forecasts to soil properties over a sparsely vegetated dryland region. *J. Appl. Meteorol. Climatol.* **2014**, *53*, 1976–1995. [CrossRef]

28. Dimitrova, R.; Silver, Z.; Fernando, H.; Leo, L.; DiSabatino, S.; Hocut, C.; Zsedrovits, T. Intercomparison between Different PBL Options in WRF Model: Modification of 2 PBL Schemes for Stable Conditions. In Proceedings of the 94th Annual Meeting of the American Meteorological Society (AMS), Atlanta, GA, USA, 2–6 February 2014; p. 7.

29. Pal, S.; De Wekker, S.; Emmitt, G. Investigation of the Spatial Variability of the Convective Boundary Layer Heights over an Isolated Mountain: Cases from the MATERHORN-2012 Experiment. *J. Appl. Meteorol. Climatol.* **2016**, *55*, 1927–1952. [CrossRef]

30. Shin, H.H.; Dudhia, J. Evaluation of PBL Parameterizations in WRF at Subkilometer Grid Spacings: Turbulence Statistics in the Dry Convective Boundary Layer. *Mon. Weather Rev.* **2016**, *144*, 1161–1177. [CrossRef]

31. Njuki, S.M.; Mannaerts, C.M.; Su, Z. Influence of Planetary Boundary Layer (PBL) Parameterizations in the Weather Research and Forecasting (WRF) Model on the Retrieval of Surface Meteorological Variables over the Kenyan Highlands. *Atmosphere* **2022**, *13*, 169. [CrossRef]

32. Cheng-Gang, W.; Ying-Jie, S.; Feng, L.; Le, C.; Jia-De, Y.; Hai-Mei, J. Comparison and analysis of several planetary boundary layer schemes in WRF model between clear and overcast days. *Chin. J. Geophys.* **2017**, *60*, 141–153. [CrossRef]

33. Cohen, A.E.; Cavallo, S.M.; Coniglio, M.C.; Brooks, H.E. A review of planetary boundary layer parameterization schemes and their sensitivity in simulating southeastern U.S. cold season severe weather environments. *Weather Forecast.* **2015**, *30*, 591–612.

34. Hong, S.-Y.; Yign, N.; Jimy, D. A new vertical diffusion package with an explicit treatment of entrainment processes. *Mon. Weather Rev.* **2006**, *134*, 2318–2341. [CrossRef]

35. Wyszogrodzki, A.A.; Liu, Y.; Jacobs, N.; Childs, P.; Zhang, Y.; Roux, G.; Warner, T.T. Analysis of the surface temperature and wind forecast errors of the NCAR-AirDat operational CONUS 4-km WRF forecasting system. *Meteorol. Atmos. Phys.* **2013**, *122*, 125–143. [CrossRef]

36. Xu, H.; Wang, Y.; Wang, M. The Performance of a Scale-Aware Nonlocal PBL Scheme for the Subkilometer Simulation of a Deep CBL over the Taklimakan Desert. *Adv. Meteorol.* **2018**, *2018*, 8759594. [CrossRef]

37. Skamarock, W.C.; Snyder, C.; Klemp, J.B.; Park, S. Vertical Resolution Requirements in Atmospheric Simulation. *Mon. Weather Rev.* **2019**, *147*, 2641–2656. [CrossRef]

38. Fernando, H.J.S. Coauthors. The MATERHORN–Unraveling the Intricacies of Mountain Weather. *Bull. Am. Meteorol. Soc.* **2015**, *96*, 1945–1967. [CrossRef]

39. Fernando, H.J.S.; Pardyjak, E.R. Field Studies Delve into the Intricacies of Mountain Weather. *EOS* **2013**, *94*, 313–315. [CrossRef]

40. Janjic, Z. *Nonsingular Implementation of the Mellor—Yamada Level 2.5 Scheme in the NCEP Meso Model*; NCEP Office Note; National Centers for Environmental Prediction: College Park, MD, USA, 2001; p. 437.

41. Grachiev, A.A.; Fairall, C.W. Dependence of the Monin—Obukhov Stability Parameter on the Bulk Richardson Number over the Ocean. *J. Appl. Meteorol.* **1996**, *36*, 406–414. [CrossRef]

42. Chen, F.; Dudhia, J. Coupling an Advanced Surface—Hydrology Model with the Penn State—NCAR MM5 Modeling System. Part I: Model Implementation and Sensitivity. *Mon. Weather Rev.* **2001**, *129*, 569–585. [CrossRef]

43. Ek, M.B.; Mitchell, K.; Lin, Y.; Rogers, E.; Grunmann, P.; Koren, V.; Gayno, G.; Tarpley, J.D. Implementation of Noah land surface model advances in the National Centers for Environmental Prediction operational mesoscale Eta model. *J. Geophys. Res.* **2003**, *108*, 8851. [CrossRef]

44. Tewari, M.; Chen, F.; Wang, W.; Dudhia, J.; LeMone, M.; Mitchell, K.; Ek, M.; Gayno, G.; Wegiel, J.; Cuenca, R.H. Implementation and Verification of the Unified NOAH Land Surface Model in the WRF Model. In Proceedings of the 20th Conference on Weather Analysis and Forecasting/16th Conference on Numerical Weather Prediction, Seattle, WA, USA, 10–16 January 2004; pp. 11–15.

45. Shin, H.H.; Hong, S.; Dudhia, J.; Kim, Y. Orography—Induced Gravity Wave Drag Parameterization in the Global WRF: Implementation and Sensitivity to Shortwave Radiation Schemes. *Adv. Meteorol.* **2010**, *2010*, 959014. [CrossRef]

46. Zangl, G. An Improved Method for Computing Horizontal Diffusion in a Sigma–Coordinate Model and Its Application to Simulations over Mountainous Topography. *Mon. Weather Rev.* **2002**, *130*, 1423–1432. [CrossRef]

47. Mlawer, E.J.; Taubman, S.; Brown, P.; Iacono, M.; Clough, S.A. Radiative transfer for inhomogeneous atmospheres: RRTM, a validated correlated—k model for the longwave. *J. Geophys. Res.* **1997**, *102*, 663–682. [CrossRef]

48. Thompson, G.; Field, P.; Rasmussen, R.; Hall, W. Explicit Forecasts of Winter Precipitation Using an Improved Bulk Microphysics Scheme. Part II: Implementation of a New Snow Parameterization. *Mon. Weather Rev.* **2008**, *136*, 5095–5115. [CrossRef]

49. Kain, J.S. The Kain–Fritsch convective parameterization: An update. *J. Appl. Meteorol.* **2004**, *43*, 170–181. [CrossRef]

50. Arthur, R.S.; Lundquist, K.A.; Olson, J.B. Improved Prediction of Cold-Air Pools in the Weather Research and Forecasting Model Using a Truly Horizontal Diffusion Scheme for Potential Temperature. *Mon. Weather Rev.* **2021**, *149*, 155–171. [CrossRef]

51. Knievel, J.C.; Bryan, G.; Hacker, J.P. Explicit Numerical Diffusion in the WRF Model. *Mon. Weather Rev.* **2007**, *135*, 3808–3824. [CrossRef]

52. Dudhia, J. Reply. *Mon. Weather Rev.* **1995**, *123*, 2573–2575. [CrossRef]

53. Janjic, Z.; Gall, R. *Nonhydrostatic Multiscale Model on the B grid (NMMB). Part 1 Dynamics*; NCAR Technical Note; University Corporation for Atmospheric Research: Boulder, CO, USA, 2012.

54. Loveland, T.R.; Merchant, J.W.; Reed, B.C.; Brown, J.F.; Ohlen, D.O.; Olson, P.; Hutchinson, J. Seasonal land cover regions of the United States. *Ann. Assoc. Am. Geogr.* **1995**, *85*, 339–355. [CrossRef]

55. Miller, D.; White, R. A Conterminous United States Multilayer Soil Characteristics Dataset for Regional Climate and Hydrology Modeling. *Earth Interact.* **1998**, *2*, 1–26. [CrossRef]

56. Fry, J.; Xian, G.; Jin, S.; Dewitz, J.; Homer, C.; Yang, L.; Barnes, C.; Herold, N.; Wickham, J. Completion of the 2006 National Land Cover Database for the Conterminous United States. *Photogramm. Eng. Remote Sens.* **2011**, *77*, 858–864.

57. Hennig, T.A.; Kretsch, J.; Pessagno, C.; Salamonowicz, P.; Stein, W. The Shuttle Radar Topography Mission. *Digit. Earth Moving. Lect. Notes Comput. Sci.* **2001**, *2181*, 65–77.

58. Environmental Modeling Center. *The GFS Atmospheric Model. NCEP Office Note 442, Global Climate and Weather Modeling Branch*; EMC: Camp Springs, MD, USA, 2003.

59. Galperin, B.; Sukoriansky, S. Progress in turbulence parameterization for geophysical flows. In Proceedings of the 3rd International Workshop on Next-Generation NWP Models: Bridging Parameterization, Explicit Clouds, and Large Eddies, Seoul, Republic of Korea, 4 May 2010.

60. Chou, M.D.; Suarez, M.J. A solar radiation parameterization for atmospheric studies. *NASA Tech. Memo.* **1999**, *40*, 104606.

61. Chou, M.D.; Suarez, M.; Liang, X.; Yan, M.M.H. A thermal infrared radiation parameterization for atmospheric studies. *NASA Tech. Memo.* **2001**, *68*, 104606.

62. McCumber, M.; Pielke, R.A., Sr. Simulation of the Effects of Surface Fluxes of Heat and Moisture in a Mesoscale Numerical Model 1. Soil Layer. *J. Geophys. Res.* **1981**, *86*, 9929–9938. [CrossRef]

63. Johansen, O. Thermal Conductivity of Soils. Ph.D. Thesis, Norwegian University of Science and Technology, Trondheim, Norway, 1975; p. 291.

64. Lehner, M.; Whiteman, C.; Hoch, S.; Jensen, D.; Pardyjak, E.; Leo, L.; Di Sabatino, S.; Fernando, H.J.S. A Case Study of the Nocturnal Boundary Layer Evolution on a Slope at the Foot of a Desert Mountain. *J. Appl. Meteorol. Climatol.* **2015**, *54*, 732–751. [CrossRef]

65. Jeglum, M.E.; Hoch, S. Multiscale Characteristics of Surface Winds in an Area of Complex Terrain in Northwest Utah. *J. Appl. Meteorol. Climatol.* **2016**, *55*, 1549–1563. [CrossRef]

66. Rodrigues, C.V.; Palma, J.M.L.M. Estimation of turbulence intensity and shear factor for diurnal and nocturnal periods with an URANS flow solver coupled with WRF. *J. Phys. Conf. Ser.* **2014**, *524*, 10. [CrossRef]

67. Massey, J.D.; Steenburgh, W.; Knievel, J.; Cheng, W. Regional Soil Moisture Biases and their Influence on WRF Model Temperature Forecasts over the Intermountain West. *Weather Forecast.* **2016**, *31*, 197–216. [CrossRef]

68. Han, L.; Ding, J.; Zhang, J.; Chen, P.; Wang, J.; Wang, Y.; Wang, J.; Ge, X.; Zhang, Z. Precipitation events determine the spatiotemporal distribution of playa surface salinity in arid regions: Evidence from satellite data fused via the enhanced spatial and temporal adaptive reflectance fusion model. *CATENA* **2021**, *206*, 105546. [CrossRef]

69. Hang, C.; Nadeau, D.; Jensen, D.; Hoch, S.; Pardyjak, E. Playa Soil Moisture and Evaporation Dynamics During the MATERHORN Field Program. *Bound. Layer Meteorol.* **2016**, *159*, 521–538. [CrossRef]

70. Jensen, D.D.; Nadeau, D.; Hoch, S.; Pardyjak, E.R. Observations of near-surface heat-flux and temperature profiles through the early evening transition over contrasting surfaces. *Bound. Layer Meteorol.* **2016**, *159*, 567–587. [CrossRef]

71. Stauffer, D.R. *Uncertainty in Environmental NWP Modeling. Handbook of Environmental Fluid Dynamics*; Harindra, J., Fernando, S., Eds.; Taylor &Francis Books, Inc.: London, UK, 2011.

72. Morrison, T.; Calaf, M.; Higgins, C.; Drake, S.; Perelet, A.; Pardyjak, E. The Impact of Surface Temperature Heterogeneity on Near-Surface Heat Transport. *Bound. Layer Meteorol.* **2021**, *180*, 247–272. [CrossRef]

73. Silver, Z.; Dimitrova, R.; Zsedrovits, T.; Baines, P.; Fernando, H. Simulation of Stably Stratified flow in complex terrain: Flow structures and dividing streamline. *Environ. Fluid Mech.* **2018**, *20*, 1281–1311. [CrossRef]

74. Massey, J.D.; Steenburgh, W.; Hoch, S.; Jensen, D. Simulated and Observed Surface Energy Fluxes and Resulting Playa Breezes during the MATERHORN. *J. Appl. Meteorol. Climatol.* **2017**, *56*, 915–935. [CrossRef]

75. Hang, C.; Nadeau, D.; Pardyjak, E.; Parlange, M. A comparison of near-surface potential temperature variance budgets for unstable atmospheric flows with contrasting vegetation cover flat surfaces and a gentle slope. *Environ. Fluid Mech.* **2020**, *20*, 1251–1279. [CrossRef]

76. Duine, G.L.; De Wekker, S. The effects of horizontal grid spacing on simulated daytime boundary layer depths in an area of complex terrain in Utah. *Environ. Fluid Mech.* **2017**, *20*, 1313–1331. [CrossRef]

77. Tijm, A.B.C.; Holtslag, A.A.M.; van Delden, A.J. Observations and Modeling of the Sea-Breeze with the Return Current. *Mon. Weather Rev.* **1999**, *127*, 625–640. [CrossRef]

78. Dimitrova, R.; Silver, Z.; Zsedrovits, T.; Hocut, C.; Leo, L.; Di Sabatino, S.; Fernando, H. Assessment of planetary boundary-layer schemes in the Weather Research and Forecasting mesoscale model using MATERHORN field data. *Bound. Layer Meteorol.* **2016**, *159*, 589–609. [CrossRef]

79. Wyngaard, J.C. Toward Numerical Modeling in the "Terra Incognita". *J. Atmos. Sci.* **2004**, *61*, 1816–1826. [CrossRef]
80. Ching, J.; Rotunno, R.; LeMone, M.; Martilli, A.; Kosović, B.; Jiménez, P.; Dudhia, J. Convectively induced secondary circulations in fine-grid mesoscale numerical weather prediction models. *Mon. Weather Rev.* **2014**, *42*, 3284–3302. [CrossRef]
81. Rai, R.K.; Berg, L.; Kosović, B.; Haupt, S.; Mirocha, J.; Ennis, B.; Draxl, C. Evaluation of the impact of horizontal grid spacing in terra incognita on coupled mesoscale–microscale simulations using the WRF framework. *Mon. Weather Rev.* **2019**, *147*, 1007–1027. [CrossRef]
82. Haupt, S.E.; Kosović, B.; Shaw, W.; Berg, L.; Churchfield, M.; Cline, J.; Draxl, C.; Ennis, B.; Koo, E.; Kotamarthi, R.; et al. On bridging a modeling scale gap: Mesoscale to microscale coupling for wind energy. *Bull. Am. Meteorol. Soc.* **2019**, *100*, 2533–2550. [CrossRef]
83. Hawbecker, P.; Kosović, B.; Muñoz-Esparza, D.; Sauer, J.; Dudhia, J.; Patton, G. Simulations Across Scales over Complex Terrain: Lessons Learned from a Perdigao Case Study. Joint WRF/MPAS Users' Workshop 2021 (Virtual), NCAR, June 2021. Available online: https://www2.mmm.ucar.edu/wrf/users/workshops/WS2021/presentation_pdfs/hawbecker.pdf (accessed on 2 December 2022).
84. Dai, Y.; Basu, S.; Maronga, B.; de Roode, S.R. Addressing the Grid-Size Sensitivity Issue in Large-Eddy Simulations of Stable Boundary Layers. *Bound. Layer Meteorol.* **2021**, *178*, 63–89. [CrossRef]
85. Seaman, N.L.; Gaudet, B.J.; Stauffer, D.R.; Mahrt, L.; Richardson, S.J.; Zielonka, J.R.; Wyngaard, J.C. Prediction of Submesoscale in the Nocturnal Stable Boundary Layer over Complex Terrain. *Mon. Weather Rev.* **2012**, *140*, 956–977. [CrossRef]
86. Paperman, J.; Potchter, O.; Alpert, P. Characteristics of the summer 3-D katabatic flow in a semi-arid zone—The case of the Dead Sea. *Int. J. Climatol.* **2022**, *42*, 1975–1984. [CrossRef]
87. Serafin, S.; Adler, B.; Cuxart, J.; De Wekker, S.; Gohm, A.; Grisogono, B.; Kalthoff, N.; Kirshbaum, D.; Rotach, M.; Schmidli, J.; et al. Exchange Processes in the Atmospheric Boundary Layer Over Mountainous Terrain. *Atmosphere* **2018**, *9*, 32. [CrossRef]
88. Lee, T.R.; Buban, M. Evaluation of Monin–Obukhov and Bulk Richardson Parameterizations for Surface–Atmosphere Exchange. *J. Appl. Meteorol. Climatol.* **2020**, *59*, 1091–1107. [CrossRef]
89. Pilotto, I.L.; Rodríguez, D.A.; Chan Chou, S.; Tomasella, J.; Sampaio, G.; Gomes, J.L. Effects of the surface heterogeneities on the local climate of a fragmented landscape in Amazonia using a tile approach in the Eta/Noah-MP model. *Q. J. R. Meteorol. Soc.* **2017**, *143*, 1565–1580. [CrossRef]
90. Arsenault, K.R.; Nearing, G.S.; Wang, S.; Yatheendradas, S.; Peters-Lidard, C.D. Parameter Sensitivity of the Noah-MP Land Surface Model with Dynamic Vegetation. *J. Hydrometeorol.* **2018**, *19*, 815–830. [CrossRef]
91. Beck, J.; Brown, J.; Dudhia, J.; Gill, D.; Hertneky, T.; Klemp, J.; Wang, W.; Williams, C.; Hu, M.; James, E.; et al. An Evaluation of a Hybrid, Terrain-Following Vertical Coordinate in the WRF-Based RAP and HRRR Models. *Weather Forecast.* **2020**, *35*, 1081–1096. [CrossRef]
92. Daniels, M.; Lundquist, K.; Mirocha, J.; Wiersema, D.; Chow, F. A New Vertical Grid Nesting Capability in the Weather Research and Forecasting (WRF) Model. *Mon. Weather Rev.* **2016**, *144*, 3725–3747. [CrossRef]